UNIVERSIDADE DE LISBOA

Faculdade de Medicina

Dynamics of triad positioning during skeletal myofiber contraction and stretching

Mafalda Araújo e Sá Pereira

Orientadores:

Doutora Ana Raquel Pereira

Prof. Doutor Edgar Rodrigues Almeida Gomes

Documento provisório

Dissertação especialmente elaborada para obtenção do grau de Mestre em Investigação Biomédica

2024

UNIVERSIDADE DE LISBOA

Faculdade de Medicina

Dynamics of triad positioning during skeletal myofiber contraction and stretching

Mafalda Araújo e Sá Pereira

Orientadores:

Doutora Ana Raquel Pereira

Prof. Doutor Edgar Rodrigues Almeida Gomes

Documento provisório

Dissertação especialmente elaborada para obtenção do grau de Mestre em Investigação Biomédica

2024

A impressão desta dissertação foi aprovada pelo Conselho Científico da Faculdade de Medicina de Lisboa em reunião de

20 de Fevereiro de 2024

Acknowledgments

I want to thank my supervisors Dra Ana Raquel Pereira and Dr Edgar Gomes, for giving me the opportunity of developing this project side by side with you. For guiding me through the ups and downs, for the great advice and for always having an encouraging word! And for the patience you showed throughout my journey at the lab.

To all the former and present members of the Edgar Gomes Lab, thank you for always being so welcoming and fun! I have learnt a great deal from every single one of you.

I look forward to keep working with you!

Thank you to all the iMM community, and to my fellow Master colleagues for being such great people and always supportive! A special thanks to the Facilities, who keep the machine well-oiled and make it possible for such great science to flourish at iMM!

Thank you to my family for supporting my path throughout this career. But a very special thanks to Pedro Tavares, who has been my rock through these years. Thank you for listening, for giving me all the good advice, for being a great cook and for always being you!

List of Abbreviations

AAV	- Adeno-associated viruses
A-band	- Anisotropic band
Ach	- Acetylcholine
ADP	- Adenosine diphosphate
ATP	- Adenosine triphosphate
C. elegans	- Caenorhabditis elegans
CAPN3	- Calpain-3
ChR2	- Channelrhodopsin-2
CMYA5	- Cardiomyopathy Associated 5
CNM	- Centronuclear myopathy
DHPR	- Dihydropyridine receptor
DT-M	- Distance between triads over M-band
DT-Z	- Distance between triads over Z-line
EC-coupling	- Excitation contraction coupling
I-band	- Isotropic band
JPH1	- Junctophilin-1
j-SR	- Junctional sarcoplasmic reticulum
KCl	- Potassium chloride
l-SR	- Longitudinal sarcoplasmic reticulum
ms	- Milliseconds
NMJ	- Neuromuscular junction
PEVK domain	- Proline, Glutamate, Valine and Lysine-rich domain
pLL-g-PEG	- Poly(L-Lysine)-grafted-Poly(Ethylene Glycol)
RYR	- Ryanodine receptor
SL	- Sarcomeric Length
SD	- Spinning disk
sec	- Second
SERCA	- Sarcoendoplasmic reticulum Ca^{2+}-ATPase
SR	- Sarcoplasmic reticulum
T-tubule	- Transverse tubule
µm	- Micrometers
WT	- Wild-type

Abstract

Skeletal muscle locomotive function relies on the contractility of sarcomeres. Sarcomeres are composed of actin cables with myosin filaments. During muscle cell contraction, plasma membrane depolarisation triggers the opening of calcium channels at the sarcoplasmic reticulum (SR), an important step for actin and myosin cross-bridging, and ultimately sarcomere shortening. To couple excitation and contraction, the network of membranes within skeletal muscle cells forms specialised structures called triads, composed of a plasma membrane invagination, the transverse tubule (T-tubule), flanked by two terminal cisternae of the SR.

In mammalian skeletal muscle, triads preferentially locate transversally at the A-I junction, the actin-myosin interface. Mislocalization of triads is a hallmark of myopathies, such as centronuclear myopathy and Duchenne muscular dystrophy. Yet, it remains unclear if triads are structurally linked to the sarcomere and, if so, is the triad positioning fixed at the A-I junction. Therefore, we performed high-speed super-resolution live-cell tracking of triads during muscle cell contraction in an optimised micropatterned *in vitro* system that facilitates single sarcomere imaging. Additionally, we conducted *ex vivo* experiments involving manual stretching and potassium chloride-induced contraction of whole skeletal muscle to address this question in fully developed muscle tissue.

Given the physiological significance of triad positioning at A-I junction, we anticipate that triads remain tethered at this region during sarcomeric length variation. Surprisingly, triads exhibited a dynamic positioning, invading the myosin filament region during shortening and distancing from it during stretching, refuting our initial hypothesis.

Further characterization of the dynamic triad localisation profile showed potential elastic movement, similar to that of Titin's N2A element. Understanding the correlation between triads positioning and sarcomeric length variation can shed light on the nature of the connection between triads and myofibrils, including associated anchoring proteins. This information is useful for the development of therapeutic interventions for myopathies characterised by triad mispositioning.

Key words: skeletal muscle, triad positioning, myofiber contraction, high speed super-resolution imaging, micropatterning

Resumo

A função locomotora do músculo esquelético depende da contratilidade dos sarcómeros, que são compostos por filamentos de actina e de miosina. Durante a contração da célula do músculo, a despolarização da membrana plasmática desencadeia a abertura de canais de cálcio no retículo sarcoplasmático (RS). A libertação de cálcio é fundamental para despoletar o deslizamento dos filamentos de actina sobre a miosina, e, consequentemente, levar ao encurtamento do sarcómero. Para acoplar a excitação e a contração, a rede de membranas que rodeia e invagina as células musculares forma estruturas especializadas chamadas tríade. Estas são compostas por uma invaginação da membrana plasmática, o tubo transversal (túbulo-T), e por duas cisternas terminais do RS de cada lado.

No músculo esquelético de mamíferos, as tríades localizam-se preferencialmente de forma transversal na junção A-I, a interface actina-miosina. A desorganização das tríades é uma característica distintiva das miopatias, como a miopatia centronuclear e a distrofia muscular de Duchenne. No entanto, permanece incerto se as tríades estão estruturalmente ligadas ao sarcómero e se o seu posicionamento é fixo na junção A-I. Para esclarecer estas questões, implementámos um sistema *in vitro* para visualizar com high-speed e super-resolução o posicionamento das tríades durante a contração muscular. Utilizámos um sistema *micropatterned* que possibilita a observação de tríades individuais mesmo durante a variação da distância sarcomérica. Além disso, conduzimos experiências *ex vivo* envolvendo alongamento manual e contração induzida por cloreto de potássio de músculo esquelético. Desta forma, abordamos as mesmas questões agora em tecido muscular totalmente desenvolvido.

Dada a importância fisiológica do posicionamento das tríades na junção A-I, nós antecipamos que estas permaneçam ancoradas nesta região durante a variação do comprimento dos sarcómeros. Surpreendentemente, as tríades exibiram um posicionamento dinâmico, invadindo a região dos filamentos de miosina durante a redução do sarcómero, e afastando-se dela quando o músculo é esticado, refutando a nossa hipótese inicial.

Uma caracterização mais detalhada do perfil de localização das tríades mostrou potenciais propriedades elásticas, semelhantes às do elemento N2A da Titina. Compreender a correlação entre o posicionamento das tríades e a variação do comprimento dos sarcómeros pode enriquecer a nossa compreensão sobre a natureza da conexão entre tríades e miofibrilas, incluindo as proteínas de ancoragem associadas. Esta informação é útil para o desenvolvimento de intervenções terapêuticas para miopatias caracterizadas por disrupção do posicionamento das tríades.

Palavras-Chave: músculo esquelético; posicionamento das tríades; contração da miofibra; *high-speed* super-resolução; *micropatterning*.

Resumo Alargado

O músculo esquelético é um componente chave na execução de funções locomotoras devido às suas propriedades intrínsecas de excitabilidade e contractilidade. Estas propriedades fundamentais são moduladas pela arquitetura celular altamente organizada do músculo. Em mamíferos, as células (ou fibras) musculares estendem-se longitudinalmente ao longo do músculo em unidades agrupadas, chamadas fascículos. Cada fibra possui milhares miofibrilas que consistem num padrão repetitivo de unidades contráteis, designadas por sarcómeros. Os sarcómeros encontram-se unidos de ponta a ponta pelas linhas Z, as quais delimitam o comprimento de cada sarcómero. No centro, a linha M ancora os filamentos de miosina, os quais se sobrepõem e intercalam com os filamentos de actina, ancorados nas linhas Z. Quando observado ao microscópio, a estrutura do sarcómero revela-se mais escura numa região central, designada por Banda A e que engloba toda a extensão dos filamentos de miosina. Simultaneamente, uma região mais clara pode também ser observada e que corresponde à Banda I, composta apenas por filamentos de actina. O alinhamento deste padrão periódico de sarcómeros ao longo da fibra produz a sua aparência estriada[1,2].

Ao nível da membrana plasmática que rodeia as fibras, invaginações membranares designadas por túbulos transversais (túbulos-T) são ladeadas de ambos os lados pelas cisternas terminais do retículo sarcoplasmático (RS), estabelecendo uma tríade[12]. A função da tríade está intimamente relacionada com o acoplamento excitação-contração (EC-coupling), onde o potencial de ação gerado pelos neurónios motores induz a despolarização ao longo da membrana plasmática, até alcançar os túbulos-T. Nesta estrutura, a depolarização da membrana ativa canais de cálcio (Ca^{2+}) dependentes de voltagem, também chamados de recetores de dihidropiridina (DHPR). Estes recetores estão fisicamente acoplados aos recetores de rianodina 1 (RyR1), expressos na membrana do RS. A sua ligação estrutural permite uma ativação rápida e sincronizada, que gera a libertação para o citosol dos iões de Ca^{2+} armazenados no RS. Isto confere velocidades de acoplamento excitação-contração elevadas, apenas observadas na contração do músculo esquelético. Ao chegar aos filamentos de actina, o Ca^{2+} induz o movimento do

complexo tropomiosina-troponina por estes filamentos, destapando os sítios de ligação miosina-actina. Inicia-se o ciclo de deslizamento da actina sob a miosina em direção ao centro do sarcómero, que termina com uma redução sincronizada dos sarcómeros e, consequentemente, com a contração da fibra muscular[27,28].

Nas fibras musculares esqueléticas de mamíferos, as tríades localizam-se preferencialmente na junção A-I, a interface da região de sobreposição dos filamentos sarcoméricos. Hollingworth, *et al* (2013) mostraram que esta posição das tríades em fibras rápidas de ratinho promove a rapidez do acoplamento excitação-contração comparativamente com as fibras de sapo, onde as tríades se localizam nas linhas Z[34]. Hipotetiza-se que este posicionamento das tríades mais próximo da região de sobreposição dos filamentos reduz a distância de difusão do Ca^{2+}, promovendo uma contração mais rápida[35]. Para além disso, a importância do correto posicionamento das tríades é também destacada pelas miopatias centronucleares (CNM), onde tríades mal posicionadas são um *hallmark* destas doenças e contribuem para fraqueza muscular observada nos pacientes[36-38]. Mutações em proteínas associadas a CNM têm complementado o nosso conhecimento sobre o mecanismo de posicionamento das tríades na junção A-I. Contudo, persiste a incerteza sobre existência de uma ligação molecular entre as tríades e as miofibrilas capaz de manter as tríades ancoradas na junção A-I.

Desta forma, o projeto visa confirmar a existência desta relação de ancoramento entre as tríades e a junção A-I. Para tal pretendemos visualizar e caracterizar o posicionamento das tríades durante eventos que estimulem a variação do comprimento do sarcómero (SL), como a indução da contração ou do alongamento da fibra muscular. Nós hipotetizamos que as tríades estejam ancoradas à junção A-I uma vez que este posicionamento acarreta grande importância fisiológica para a funcionalidade do músculo. Assim, esperamos observar a distância entre tríades do mesmo sarcómero inalterada durante a variação do SL. Neste sentido, propomos estabelecer um sistema *in vitro* para obter fibras musculares esqueléticas primárias de ratinho, maduras e contráteis, implementar uma abordagem de estimulação de contração neste sistema para induzir contração sincronizada das fibras, e alcançar

live-cell imagens de super-resolução temporalmente resolvidas das tríades de cada sarcómero individual.

Primeiro realizámos *micropatterning* do nosso sistema *in vitro* para alinhar e individualizar fibras, por forma a diminuir potenciais artefactos durante o *live-cell imaging*. Estas fibras demonstraram todas as características de maturação: linhas Z e M transversais (estriação), núcleos à periferia e tríades transversais. A seguir, testámos a sua contractilidade implementando uma abordagem optogenética de estimulação de contração. Infelizmente, no nosso sistema a estimulação optogenética não produziu contração de fibras significativa. Deste modo, construímos um sistema *homemade* de estimulação por campo elétrico. Com esta abordagem elétrica, foi possível modular da frequência e duração das contrações, possibilitando um melhoramento da resolução espacial e temporal em *live-cell imaging*. Curiosamente, nas nossas culturas primárias, após estimulação, a maioria das fibras observadas aumentaram o seu SL, em vez de diminuírem como era esperado após estimulação de contração.

Desta forma, obtivemos tanto diminuição como aumento do sarcómero, sendo possível estimular eletricamente tanto contração como alongamento das fibras *in vitro*. A partir do *live-cell imaging* pudemos analisar o posicionamento das tríades em sarcómeros individuais e a sua tendência geral. Verificámos que as tríades pertencentes ao mesmo sarcómero apresentavam menor distância entre elas durante a contração, e aumentavam durante o alongamento. A distância entre tríades de sarcómeros adjacentes manteve-se relativamente constante. Estes dados refutam a nossa hipótese inicial, indicando que as tríades não estão ancoradas à junção A-I, mas poderão estar a outra estrutura do sarcómero, visto que se movem em concordância com o mesmo. Porém, a análise de sarcómeros individuais realçou uma heterogeneidade no posicionamento das tríades durante a estimulação da fibra.

Por esse motivo, decidimos realizar experiências *ex vivo* envolvendo alongamento manual e contração induzida por cloreto de potássio de músculo esquelético de ratinho. Assim, tivemos a possibilidade de abordar as mesmas questões num tecido

totalmente desenvolvido *in vivo*. Com estas experiências *ex vivo* obtivemos resultados semelhantes aos *in vitro*: a distância entre as tríades do mesmo sarcómero variava positiva e linearmente com a variação do SL. Por outro lado, o perfil da distância entre tríades de sarcómeros adjacentes mostrou-se um pouco diferente do que foi observado *in vitro*, provavelmente por termos um maior intervalo de SLs. Para esta distância verificámos inicialmente um aumento da sua correlação com o SL, mas depois de delimitado o intervalo de SLs fisiológicos apercebemo-nos que esta se mantém relativamente constante, como visto anteriormente *in vitro.* Fora desse intervalo fisiológico, a distância entre tríades de sarcómeros adjacentes diminui abaixo deste e tende a aumentar um pouco acima, sugerindo um comportamento elástico semelhante à correlação previamente observada entre a distância da linha Z e o domínio da Titina N2A com as variações do SL[98].

Além disto, algumas inferências também puderam ser feitas em relação ao RS. Visto que as tríades demostraram variação de distância assimétrica entre tríades do mesmo sarcómero versus tríades de sarcómeros adjacentes, podemos paralelamente inferir que o RS sob a linha M poderá ser mais elástico, sendo que esta região do RS também encolhe e estica com as tríades. Em contrapartida, o RS sob a linha Z poderá ser mais rígido, uma vez que as tríades de sarcómeros adjacentes são capazes de manter a distância entre elas mais constante.

Em suma, com este projeto estabelecemos um sistema *in vitro* de imagem em tempo real, de alta velocidade e super-resolução para acompanhar o movimento das tríades durante eventos dinâmicos, como contração da fibra. Embora tenhamos enfrentado desafios, especialmente no que diz respeito ao posicionamento transversal das tríades, as experiências *ex vivo* forneceram informações cruciais sobre o seu posicionamento relativo ao sarcómero: as tríades não estão ancoradas à junção A-I, mas as semelhanças entre a correlação das tríades e do domínio N2A com a variação SL levanta a possibilidade de que as tríades possam estar ancoradas ao elemento N2A da Titina, mediadas por interações entre RYR1, CMYA5 e CAPN3. Estudos futuros baseados nestas descobertas têm o potencial de avançar a nossa compreensão sobre as interações entre membranas-sarcómero

e potencialmente ajudar na formulação de novas terapias para pacientes com CNM ou outras distrofias afetadas por desorganização das tríades.

Index

1. Introduction

1.1. Skeletal muscle structure and biology

Muscle tissue, with its remarkable ability to convert energy into movement, presents a variety of functions, from pumping blood to supporting heavy weightlifting or childbirth. It is further categorised into two main types: smooth and striated muscles, based on the internal arrangement of their contractile filaments. **Smooth muscles** reside within hollow organ walls and do not present a regular organisation of contractile units. In **striated muscles** this organisation is evident, even under a brightfield microscope. Their predominant location is at the heart and attached to the skeleton[1].

Within **striated muscle** further distinction can be delineated between cardiac and skeletal muscles. Although sharing a similar contractile apparatus architecture, these muscles diverge significantly in both function and cellular structure. **Cardiac muscle** comprises elongated mononucleated cells interconnected by specialised intercalated disks, contributing to the involuntary heartbeat. **Skeletal muscle** is composed of bundles with long multinucleated cells capable of governing voluntary movements, body posture, and heat generation[1].

Delving deeper into skeletal muscle organisation, each muscle is intricately connected to the skeleton through tendons at each end and receives innervation from nerve fibers responsible for transmitting neuronal inputs. Layers of connective tissue envelop the muscle, with the first layer being the **epimysium** that surrounds the whole muscle. The **perimysium** encapsulates fascicles, and the **endomysium** envelopes individual skeletal muscle cells, also known as **myofibers**.

Myofibers are composed of **myofibrils**, which are rodlike contractile elements running parallel to each other along the length of the muscle cells. Within each myofibril, the basic contractile units – the **sarcomeres** – are connected end-to-end

in series, which allows for the coordinated contraction and extension, fundamental to muscle movement[1] (Figure 1).

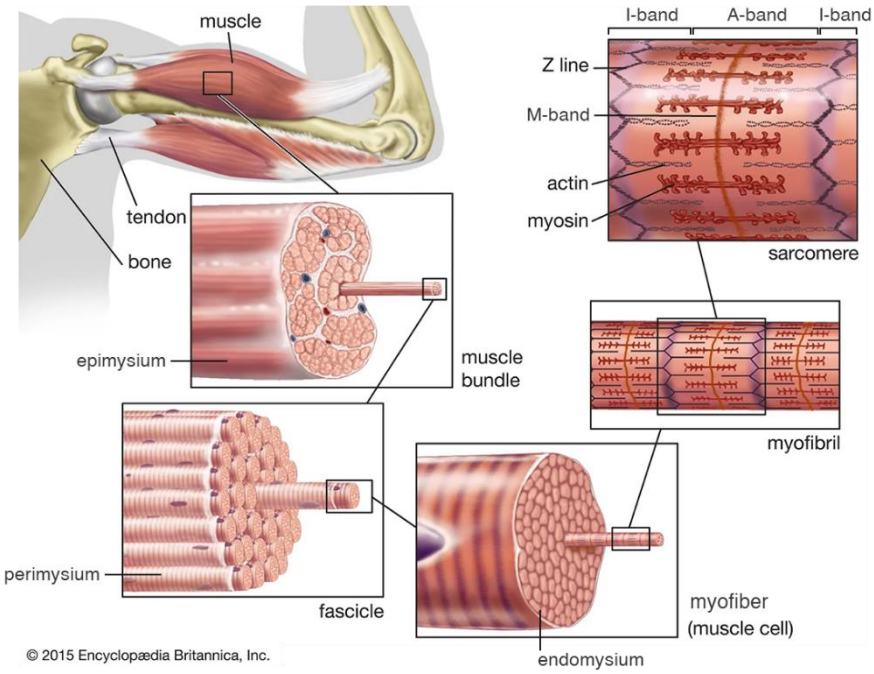

Figure 1. Hierarchical structure of skeletal muscle.
Illustration of skeletal muscle structure, which can be seen attached to the bone through the tendon. Skeletal muscle is composed by bundles of fascicles, which are themselves comprised of multiple elongated muscle cells, also known as myofibers. Each myofiber has numerous myofibrils that contain the contractile elements of the muscle – the sarcomeres. These are delineated by the Z-lines and are attached in series, running in parallel to each other along the length of the myofiber. One sarcomere displays actin filaments (thin filaments) anchored at the Z-lines, and myosin filaments (thick filaments) at the central region of the sarcomere, known as M-band. The region that spans the myosin filaments is designed as A-band, while the I-band comprises the regions where only actin filaments are present. Adapted from Encyclopædia Britannica (2023).

1.1.1. Sarcomere architecture

In striated muscles, the alternating dark and light bands observed under the microscope correspond to different regions of the sarcomere. The **A-band**, appearing as the dark region, is defined by the span of **thick filaments** which are composed of myosin. This region maintains a constant length during muscle contraction and relaxation. The **I-band**, visible as the lighter region, encompasses the **thin filaments** which consist of filamentous actin (F-actin)**.** During contraction,

this band is seen shortening. The interface where these sarcomeric filaments overlap is called the **A-I junction**[2].

Sarcomeres display a highly organised structure, with several key proteins contributing to its function and structure (Figure 2). **Actin filaments**, anchored at **Z-lines**, interact with myosin filaments to drive contraction. **Myosin filaments**, centred at the **M-band**, feature protruding heads that form ATP-driven cross-bridges with actin during myofiber contraction. Key regulatory proteins, including tropomyosin and troponin C, modulate the actin-myosin interaction. **Tropomyosin** stabilises the thin filament and along with **troponin C** controls the myosin binding sites on actin. **Nebulin** serves as a molecular ruler for actin filaments, dictating their length, while **tropomodulin** stabilises these filaments by capping their pointed ends[3,4]

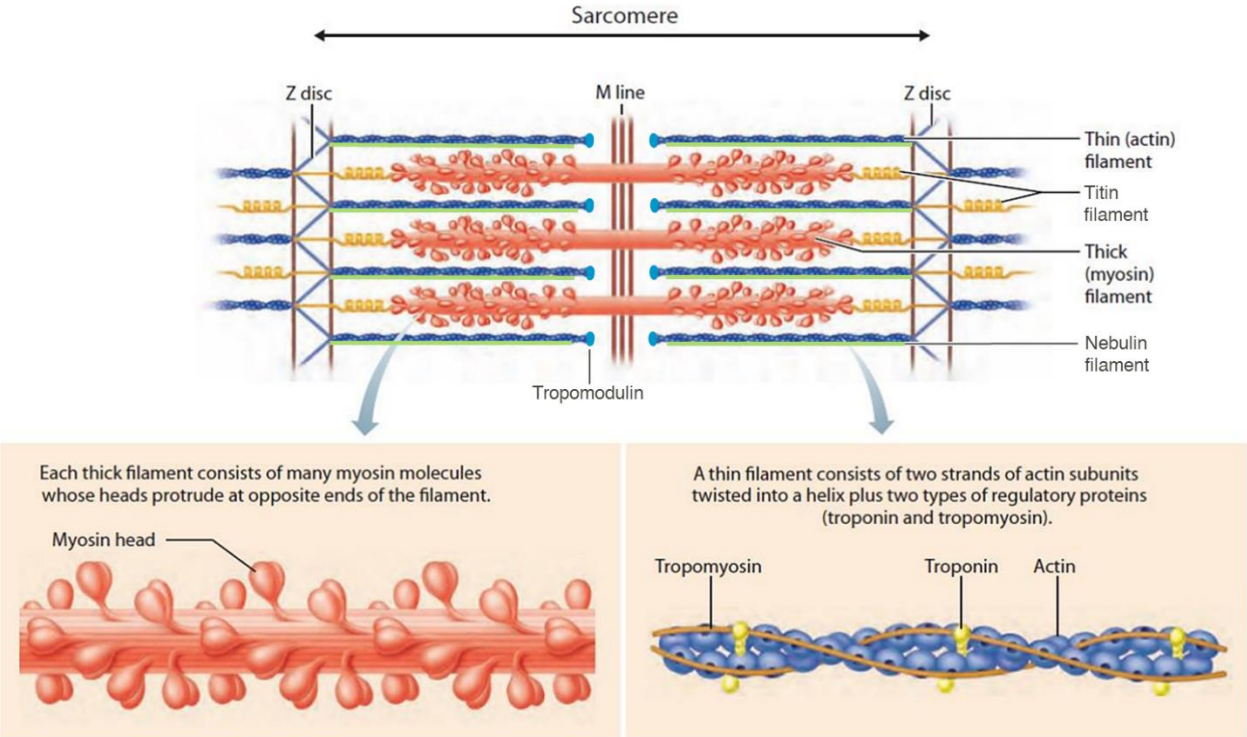

Figure 2. Sarcomere composition and organisation.

Besides the intercalated actin and myosin filaments, which are tethered at the Z-lines and M-band, respectively, other components are involved in the sarcomere structure. Key regulatory proteins modulate actin-myosin interaction sites, such as tropomyosin and troponin. Nebulin serves as a molecular ruler for actin filaments, dictating their length, while tropomodulin stabilises these filaments by capping their pointed ends. The giant protein Titin spans half of the sarcomere and keeps the myosin filaments in place, conferring resistance to stretch with their elastic properties. Adapted from Marieb and Hoehn (2007).

The giant protein **Titin**, considered the third sarcomeric filament, extends from the Z-line to the M-band of each half-sarcomere, providing structural support and elasticity, functioning as a molecular spring. The elasticity of titin is primarily attributed to its I-band region, which consists of four springlike elements: tandem immunoglobulin (Ig) domains, the PEVK domains, an N2A element (present in all striated muscles) and an N2B element (exclusive of cardiac muscle)[5,6]. Conversely, A-band region is highly repetitive and relatively inextensible (reviewed in Gregorio, et al (1999)[7]). On the other hand, Titin's A-band region guides the precise positioning and length of thick filaments, acting like a molecular blueprint of sarcomere architecture[8,9].

Desmin, an intermediate filament, provides alignment and structural linking of sarcomeres through the Z-lines[10]. **Obscurin** is known to contribute to the organisation of the sarcoplasmic reticulum and its link to the sarcomere[11].

1.1.2. Membrane network and triad structure

Surrounding each myofibril, an intricate network of membranes plays a crucial role in the coordination and regulation of muscle contraction. A specialised version of the endoplasmic reticulum known as the **sarcoplasmic reticulum** (SR) primarily stores and regulates the release of calcium ions (Ca^{2+}). The plasma membrane, also called sarcolemma, features invaginations – **transverse tubules** (T-tubules) – that penetrate deep into the cytoplasm/sarcoplasm, at specific regions of the sarcomere. Central to this network are the specialised structures known as **triads**, pivotal for excitation-contraction coupling in skeletal muscle (explained in section 1.1.3.). A triad is formed by the close association of a T-tubule with two terminal cisternae of the SR, aligning at the **A-I junction** (Figure 3). Cardiac muscle exhibits dyads, which instead are comprised of only one SR terminal cisternae and are located at the Z-lines[12–14].

Connecting the T-tubule to the SR terminal cisternae is a key protein called **Junctophilin 1** (JPH1). In skeletal muscle, JPH1 maintains the structural integrity of triads and facilitates the correct positioning of receptors involved in the excitation-

contraction coupling at the triadic membranes[15,16]. In JPH1 knockout (KO) mice, skeletal muscles exhibit severe triad abnormalities, with swollen terminal cisternae and deficient muscle contraction[17,18].

In addition to JPH1, various other proteins collaborate in T-tubule biogenesis and triad maintenance in both cardiac and skeletal muscle. **Caveolin 3** (CAV3), **Amphiphysin 2** (BIN1) and **Dysferlin** (DYSF) initiate membrane curvature, stimulate invagination and tubulation[19,20]. Additionally, the correct transversal positioning and stabilisation of T-tubules and, consequently, of triads is coordinated by proteins like **Dynamin 2** (DNM2), **Myotubularin** (MTM1) and **Mitsugumin 29** (MG29)[20–23].

Triad

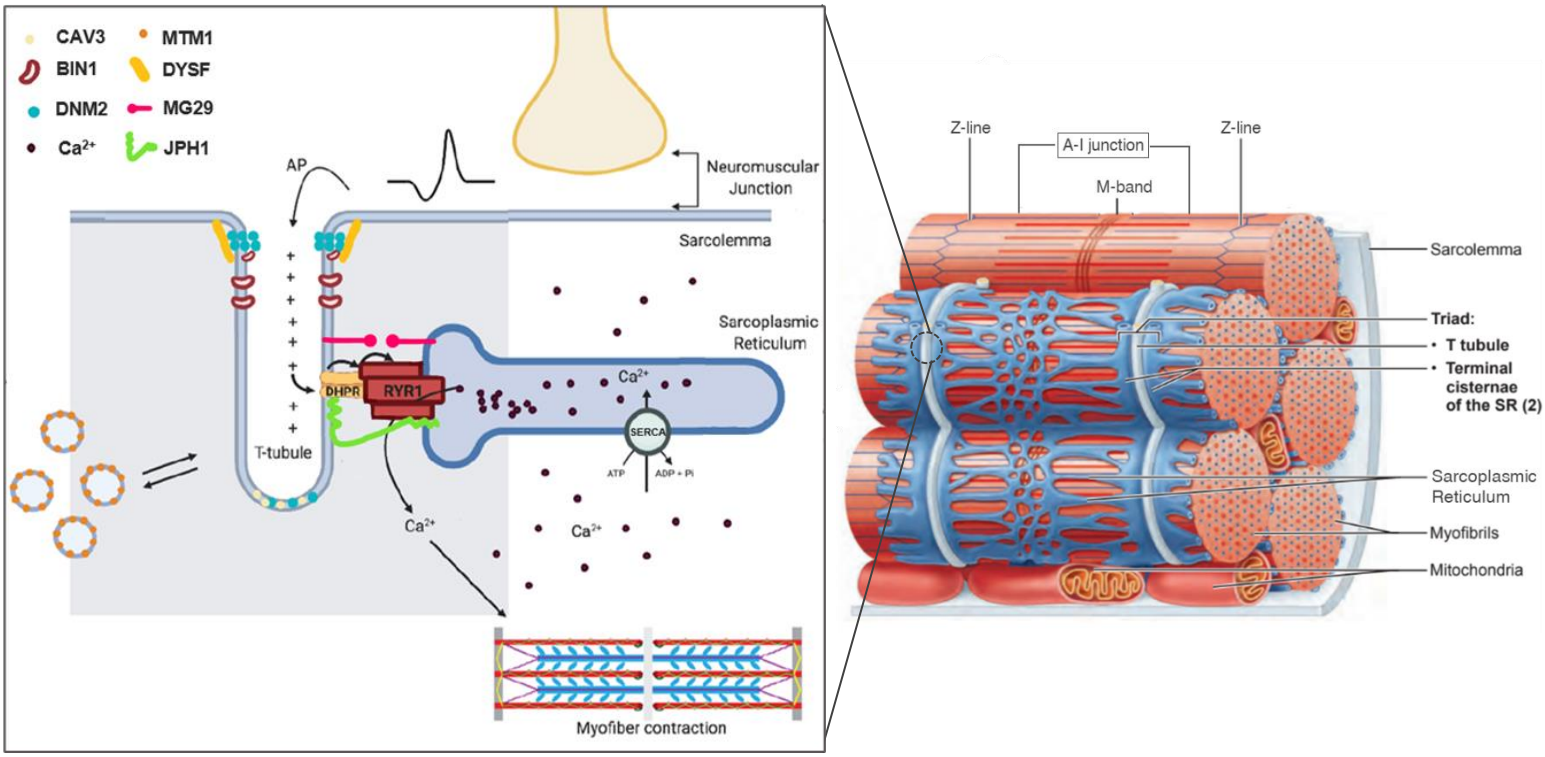

Figure 3. Triad structure in mammalian skeletal muscle.

In mammals, triads preferentially locate at the A-I junction, the interface between the overlapping sarcomeric filaments. Triads are membrane structures that surround and invaginate the myofibers, composed of one T-tubule flanked by two terminal cisternae of the sarcoplasmic reticulum (SR). Proteins such as CAV3, BIN1, DYSF and JPH1 are known to be involved in T-tubule/triad formation, while others like MTM1, DNM2 and MG29 are important for its maintenance. Triads are crucial for excitation-contraction coupling where the neuronal action potential depolarises the myofiber membrane (sarcolemma) reaching the T-tubule. Here, the dihydropyridine receptor (DHPR) are activated and trigger the opening of the ryanodine receptors (RyR1), located at the SR. This leads to SR-stored calcium release, allowing actin-myosin cross-bridging and subsequent myofiber contraction. The sarcoendoplasmic reticulum calcium ATPases (SERCA) reuptake the calcium at the cytosol after membrane repolarization, terminating contraction. Adapted from Marieb and Hoehn (2007) and from Dowling, et al (2021).

The SR displays remarkable structural specialisation within the sarcomere. The longitudinal SR (l-SR), extending along the sarcomere, primarily regulates Ca^{2+} transport and sequestration. In contrast, the **junctional SR** (j-SR), composed of the terminal cisternae, is integral for the rapid release of Ca^{2+} from the triads during contraction. The j-SR is located at the A-I junction in skeletal muscle and at the Z-lines in cardiac. Furthermore, the SR shows asymmetrical structural characteristics depending on its location within the sarcomere. Overlying the M-band, the SR forms fenestrated collars, while in the region over the Z-lines it constitutes a tubular network[24].

1.1.3. Excitation-contraction coupling

In skeletal muscle, the voluntary generation of force is initiated by an action potential from the motor neuron that reaches the **neuromuscular junction** (NMJ) and initiates the **excitation-contraction coupling** (EC-coupling), a process where the neuronal electrical signals are translated into muscle contractions.

At the NMJ, motor-neurons release **acetylcholine** (ACh) which binds and opens **voltage-gated sodium** (Na^+) **channels** at the myofiber postsynaptic membrane, initiating local membrane depolarization. This depolarization wave propagates along the T-tubules, activating voltage-gated Ca^{2+} channels known as **dihydropyridine receptors** (DHPRs). The DHPRs are structurally coupled with **ryanodine receptors** (RyR1s) located at the j-SR membrane. This structural connection between DHPRs and RyR1s is critical for rapid signal transduction, as the activation of DHPRs directly triggers the opening of RyR1s[25,26]. Consequently, Ca^{2+} is released from the SR into the cytosol, inducing conformational changes in tropomyosin–troponin complex at the thin filaments, and uncovering the actin-myosin binding sites. Myosin heads, present at the thick filaments, are now able to attach to these exposed binding sites, due to the hydrolysis of adenosine 5'-triphosphate (ATP) into adenosine 5'-diphosphate (ADP) and inorganic phosphate (Pi). Upon actin binding, Pi is released from myosin heads, changing their conformation in a power stroke motion that pulls the actin filaments towards the centre of the sarcomere. Subsequently, ADP is

replaced by ATP, causing the sarcomeric filaments to detach and allowing this **cross-bridge cycle** to repeat (Figure 4). Myofiber contraction ends with membrane repolarization and the reuptake of calcium into the SR via **sarcoendoplasmic reticulum calcium ATPases** (SERCAs)[27–29].

The cross-bridge cycle effectively generates force and results in the shortening of the sarcomere, which can be measured as the distance between adjacent Z-lines, also referenced as **Sarcomeric Length** (SL). The quantifiable reduction in SL can be used as a direct indicator of muscle contraction, providing a measurable parameter for assessing myofiber activity (Figure 4)[30–32].

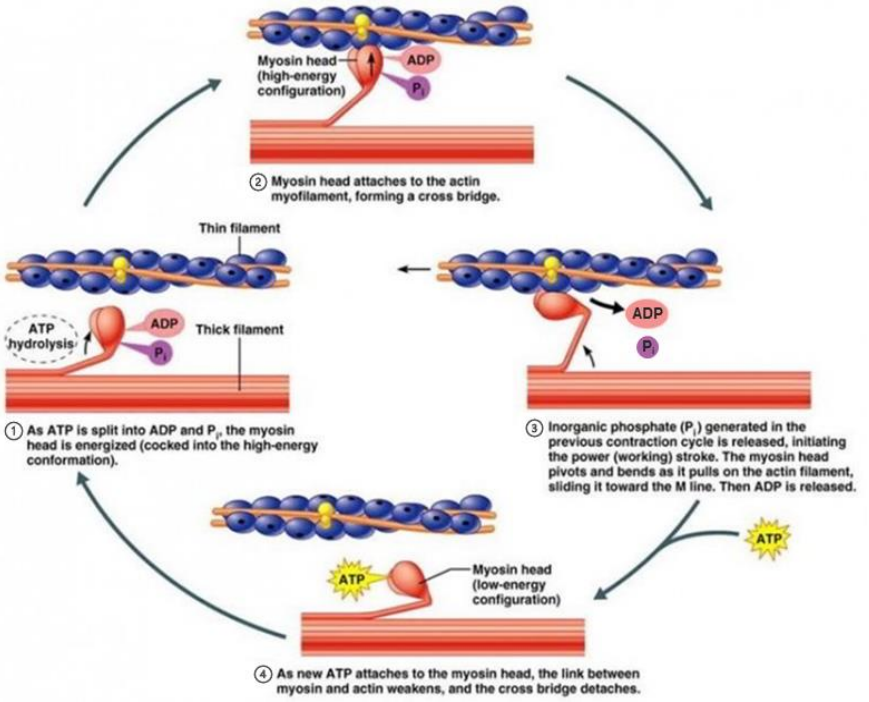

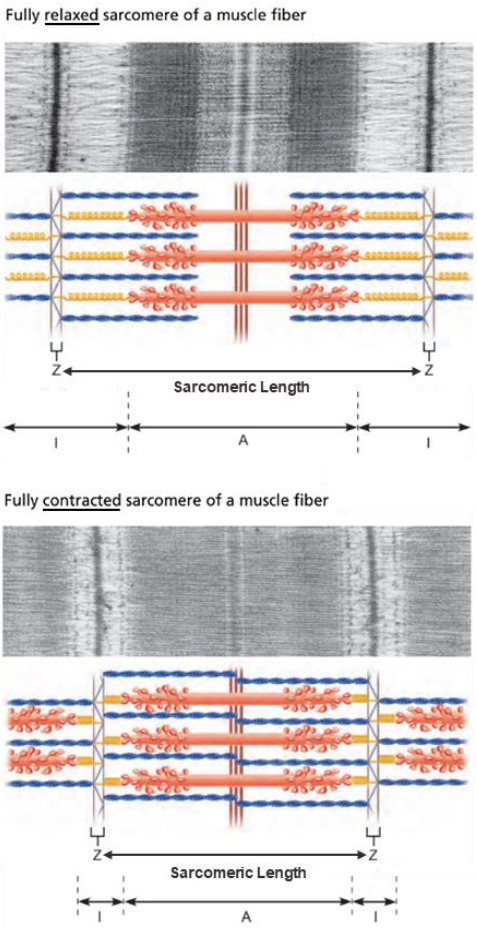

Figure 4. Actin and myosin filaments cross-bridge cycle causing Sarcomeric Length (SL) reduction during myofiber contraction.

During myofiber contraction and after calcium release, the cross-bridging cycle between actin and myosin filaments initiates to generate muscle force. The mechanism is further explained in the section 1.1.3. With the cross-bridge cycle, the actin filaments slide through the myosin filaments towards the M-band. Since actin filaments are anchored at the Z-lines, sarcomeres shorten in length to accompany actin movement. Thus, the distance between Z-lines – the Sarcomeric Length – can be used as a measure of myofiber contraction. When sarcomeres shorten, the I-band reduces in length due to the invasion of actin filaments into the myosin region. The A-band retains its width, since it delineates the myosin filaments that remain tethered at the M-band. This is illustrated through both schematic figure and electron microscopy images of relaxed and contracted skeletal myofibers. Adapted from Marieb and Hoehn (2007)

1.2. Triad positioning in mammalian skeletal myofibers

In mammals, the formation and positioning of triads within skeletal myofibers is a finely tuned and sequential process. As detailed in Franzini-Armstrong, *et al.* (2001), it is initiated with the differentiation of the SR into the j-SR, which transversally aligns near the A-I junction during embryonic development. This early phase is marked by the incorporation of key triad coupling proteins into the j-SR, highlighting the beginning of triad formation. Although T-tubule development starts simultaneously with the SR, its alignment at the A-I junction actually represents the final step in triad formation. During embryonic stages, T-tubules predominantly maintain a longitudinal orientation, transitioning to a transversal alignment at the A-I junction only postnatally[33]. This time-sensitive organisation of the triadic membranes may give further hints to the understanding of the mechanism behind triad positioning, which remains largely unknown.

Furthermore, comparative studies across species have shed light on how triad positioning within the sarcomere may influence the speed of EC-coupling events[34,35]. For instance, mouse fast-twitch myofibers display faster rates of Ca^{2+} release and reuptake upon action potential, compared to frog single-twitch myofibers. In mice, the triads are located at the A-I junction, whereas in frogs, they are positioned at the Z-lines. Hollingworth, *et al.* (2013) proposed that triad localisation at the A-I junction in mammalian myofibers, proximal to the overlapping

filaments, potentially reduces the diffusion distance for Ca^{2+} to reach troponin C, thereby promoting quicker contraction rates.

The importance of correct triad positioning becomes evident in the context of centronuclear myopathies (CNM). These congenital onset muscle diseases, characterised by central nuclei, myofiber hypotrophy, and organelle disorganisation, also feature triad mislocalization as a hallmark. This is believed to be the key contributor to the observed muscle weakness[36–38]. Triad misalignment occurs due to molecular disruptions that hinder the formation, interaction, or transversal alignment of triadic structures at the A-I junction.

One notable example is the X-linked myotubular myopathy (XLMTM), where mutations occur in the X chromosome-linked MTM1 gene. Although the molecular mechanism is not completely known, MTM1 is involved in the stabilisation of T-tubules/triads via the intermediate filament Desmin[39]. Affected patients exhibit an unusual increase in longitudinally-oriented T-tubules, reminiscent of the embryonic developmental stages seen before the final step of T-tubules/triads transversal alignment. They also present decreased levels of DHPRs and RyRs, consequently showing deficient EC-coupling and profound muscle weakness[21].

These phenotypes also extend to other forms of CNM, such as autosomal CNM caused by dominant mutations in DNM2. These mutations usually result in DNM2 overexpression and excessive functionality, causing premature or inappropriate T-tubule fission. Yet, clinical severity is somewhat milder when compared to other CNMs[40,41]. In rare BIN1-related CNM, recessive mutations result in protein loss of function. Since BIN1 is responsible for sarcolemma tubulation during T-tubule formation, this recessive CNM is characterised by the absence of functional triads[42–44].

While it is recognised that proteins like MTM1, DNM2, and BIN1 are somehow implicated in triad positioning, the exact mechanisms guiding triad alignment at the A-I junction in mammalian skeletal muscle remain elusive. This uncertainty extends to whether there even exists a molecular link that consistently tethers triads to the myofibrils at this junction. If so, triads should remain at this same position during SL

changes that occur with myofiber contraction (Figure 5). To address these gaps in knowledge, we propose to implement an *in vitro* system that facilitates live-cell imaging of triads within single sarcomeres, during induced myofiber contraction. This approach will enable the tracking of triads during active changes in SL, shedding light on their positioning in relation to the A-I junction.

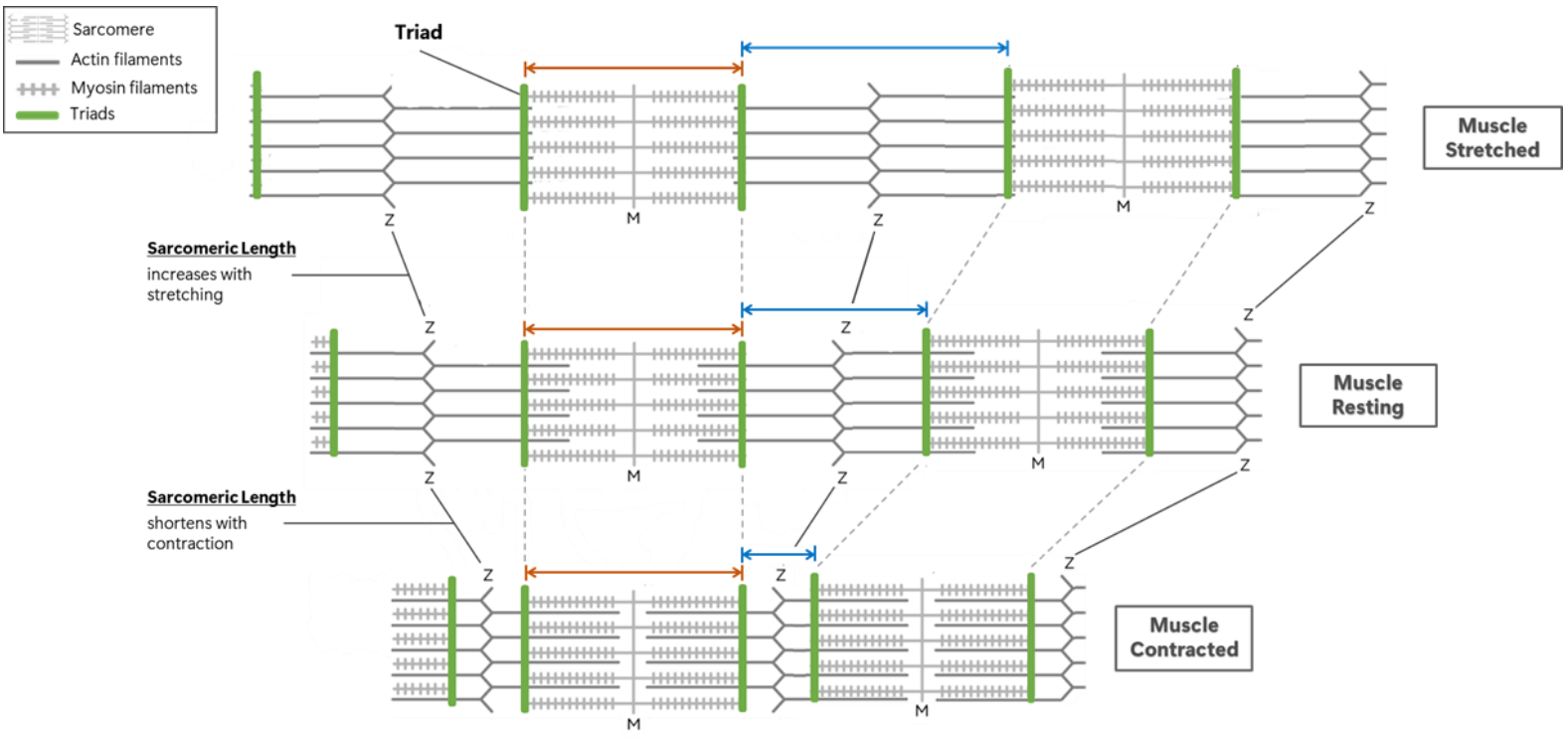

Figure 5. Conceptual model illustrating our initial hypothesis on triad positioning in mammalian skeletal muscle during stretching and contraction.

In mammalian skeletal muscle, it is known that triads locate at the A-I junction, the interface of actin and myosin filaments overlapping region, and their correct positioning at this region is important for skeletal muscle health. Yet, it remains unclear if triads are structurally linked to the sarcomere and, if so, is the triad positioning fixed at the A-I junction. Being our initial hypothesis that triads are tethered at the A-I junction, we expect that the distance between triads from the same sarcomere remains unaltered even after myofiber contraction or stretching. This way, the distance between triads from adjacent sarcomeres would decrease and increase, respectively, along with the length of the sarcomeric I-band. Two sarcomeres stretching, resting and contracting (from top to bottom) are represented along with the triad positioning and tethering at the A-I junction.

1.3. Skeletal myofiber research models

Research in skeletal muscle biology requires the integration of different research models for the deeper understanding of its development, cellular architecture, and dynamic functioning in both physiology and pathology. While *in vivo* models grant the advantage of a holistic view of skeletal muscle biology within the organism, their complexity hinders the ability of observing subcellular dynamics. *In vitro* systems offer a controlled and simplified environment for precise manipulation and direct observation of subcellular processes.

Falcone, *et al* (2014) and Pimentel, *et al* (2017) established an improved *in vitro* system where primary neonatal mouse myoblasts can be differentiated into highly mature myofibers with sarcomere alignment (transversal Z-lines and M-band), peripheral nuclei, transversal triads and twitching capability[45–48]. This differentiation is induced by serum starvation, which inhibits proliferation and promotes the development of contractile myofibers. The use of Matrigel as a substrate in this system is particularly advantageous, since its stiffness and composition closely mimic that of the extracellular matrix from *in vivo* skeletal muscle[49–52]. To prevent myofiber detachment during contraction, these are covered in a topcoat of Matrigel, improving long-term culture stability. Additionally, this system facilitates genetic manipulation of myofibers, providing further understanding of the molecular mechanisms driving myofiber development, organisation, and pathology.

The overall design of this *in vitro* model offers an ideal platform for live-cell imaging of skeletal myofibers dynamic processes, such as the movement of nuclei towards the myofiber periphery[45]. Studying the dynamics of triad positioning during myofiber contraction can also benefit from this system. However, myofibers often overlap and move in different directions during contraction stimulation, which can hinder imaging results. To overcome this limitation, micropatterning techniques can be employed in *in vitro* myofiber cultures to promote their parallel orientation, presumably enhancing their directional contraction in response to stimulus[53,54].

1.3.1. Micropatterning techniques for alignment of *in vitro* myofibers

Micropatterning techniques for *in vitro* cultures have enabled the manipulation of cell culture substrate topography, which significantly influences cell distribution and the directionality of growth. For example, introduction of a parallel array of microgrooves to a substrate has shown to effectively promote myofiber unidirectional alignment, mimicking the natural cellular arrangement found in skeletal muscle tissue and improving myofiber maturation and functionality[55,56].

Some micropatterning techniques provide a simple and reproducible mechanism to create the desired patterns in cell cultures. Among these, deep-ultraviolet (UV) based micropatterning stands out for its accessibility to standard biology labs and micron-scale precision[57,58]. This approach leverages deep-UV light to oxidise specific regions on a non-adhesive polymer layer, creating patterned cell-adhesive regions. A custom-designed photomask guides the deep-UV light and ensures the precision of pattern layout. It also simplifies the substrate patterning process for virtually any cellular geometry intended for cultures.

Therefore, this can be an advantageous technique for skeletal myofiber alignment and individualisation within an *in vitro* system. This spatial organisation of myofibers in culture can improve imaging of dynamic subcellular processes that occur during myofiber contraction.

1.3.2. *In vitro* stimulation approaches to induce myofiber contraction

In vitro skeletal myofibers can be modulated to exhibit either a twitch contraction, where an isolated action potential is elicited by a single-pulse stimulus, or a tetanic contraction, where myofibers can not relax due to the high frequency of in series pulses[59]. In both cases and based on the cross-bridge cycle theory (explained in section 1.1.3.), upon stimulation, myofibers are expected to display a uniform shortening of its sarcomeres - “synchronous” contraction.

Stimulation of myofiber contraction can be achieved through a variety of techniques, including chemical, electrical and optogenetic methods.

Chemical stimulation, although straightforward, generally leads to widespread myofiber contraction with limited temporal control. Common agents used include acetylcholine (ACh), a neurotransmitter that triggers action potentials through ACh receptors activation[60]; caffeine that facilitates calcium release from the sarcoplasmic reticulum[61]; or potassium chloride (KCl), which induces membrane depolarisation of T-tubules[62].

Electrical field stimulation, a traditional approach for collective *in vitro* myofiber contraction, offers a more versatile modulation of this event. This technique involves the strategic placement of two parallel electrodes above myofibers, connected to a stimulator, generating an electrical field that triggers membrane depolarization and, thus, myofiber contraction. This setup allows for some modulation of contraction's intensity and pattern, be it a twitch or tetanic response, according to the pulse duration, frequency, and amplitude[63]. However, since it activates all myofibers simultaneously, there could be an increased myofiber fatigue. Moreover, to track single-sarcomere events, collective myofiber activation may result in their movement beyond the field of view during live-cell imaging. Therefore, other approaches have been proposed to increase spatial resolution of myofiber activation.

Optogenetic stimulation involves genetically modifying myofibers to express light-sensitive proteins, such as Channelrhodopsin-2 (ChR2). When photo-stimulated with blue light (460-470 nm), ChR2 allows for cation entry which leads to plasma membrane depolarization and, in turn, myofiber contraction. The precise frequency and duration of the blue light pulses determines when and for how long the myofiber contracts[64].

In contrast to electrical stimulation, an optogenetic approach could offer a more refined method to selectively activate single myofibers, avoiding general myofiber fatigue in culture and potential imaging artefacts from adjacent cells' contraction. Selective activation of single myofibers has been previously accomplished using a blue LED in C2C12 cultures (immortalised mouse myoblast cell line) expressing ChR2[65].

1.4. Demands of dynamic imaging of triads during myofiber contraction

Understanding the dynamics of triad positioning during myofiber contractions requires advanced imaging techniques. Key characteristics include high temporal and spatial resolution to capture live-cell fast myofiber contraction events, which occur within 20-10 ms[66,67], and resolve triad positioning within a single sarcomere, given the ~80 nm of width observed in mammalian skeletal myofibers triads[68].

High speed live-cell imaging can be easily achieved with spinning disk confocal microscopy, where a rotating disk with multiple pinholes blocks the transmission of out-of-focus light and achieves fast fluorescence imaging with reduced phototoxicity. Unfortunately, the lateral resolution measured through full width at half maximum (FWHM) is around 200 nm for spinning disk microscopy, more than twice the width of triads[69]. Thus, super-resolution (SR) techniques should be prioritised for imaging of these subcellular structures along with the high-speed requirement.

Instant structured illumination microscopy (iSIM) provides super-resolution imaging with a lateral resolution of about 140 nm and high-speed acquisition with frequency up to 100 Hz. However, iSIM requires high signal-to-noise ratio of the fluorescent probes to facilitate clear super-resolution live-cell imaging of cellular dynamic events, such as myofiber contraction[70,71].

Laser scanning confocal microscopy with Zeiss Airyscan technology combines super-resolution imaging (lateral resolution ~120 nm) with high-speed and minimal phototoxicity. It achieves this by using a 32-element array of hexagonal detectors, which combined with advanced image reconstruction algorithms, leads to an improvement in both resolution and signal-to-noise ratio. Furthermore, the Airyscan Multiplex SR modes, such as 4Y or 8Y, use parallelization of laser scanning, which divides the laser's path into four or eight laser beams at a time, significantly speeding up acquisition time. Using Airyscan Multiplex SR mode is particularly advantageous for live-cell imaging, since it balances high-speed and super-resolution with a diminished risk of specimen photodamage[72,73].

The pursuit of effective live-cell imaging of triads during myofiber contraction displays challenging requirements, where focusing on one aspect often leads to compromises in others. These complex interplays and trade-offs can be visualised in an adapted Pyramid of Frustrations (Figure 6)[74]. At its vertices, the pyramid summarises the essential aspects: achieving optimal temporal and spatial resolution, ensuring an appropriate signal-to-noise ratio from protein labelling, appropriate myofiber maturation, and, ultimately, attaining synchronous myofiber contraction with measurable sarcomere shortening. To accomplish the objectives proposed within this project, one should aim to find a balance at the centre of the pyramid, at equal distance from the vertices.

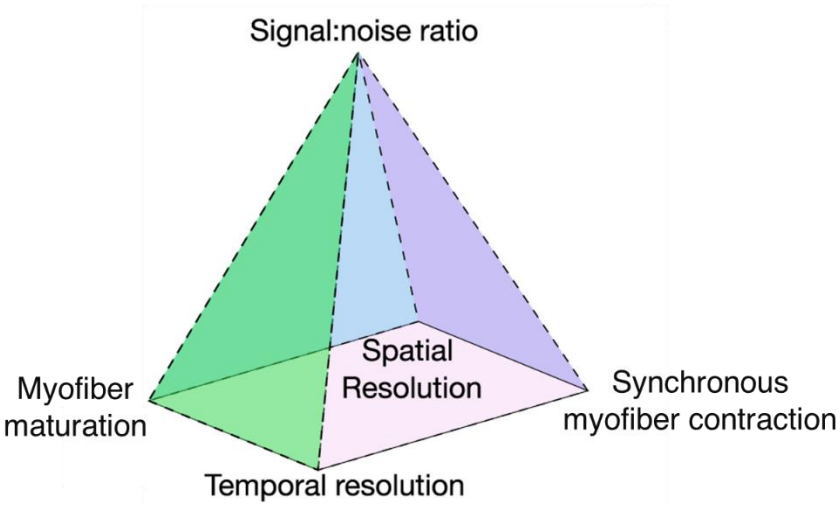

<u>Figure 6.</u> Demands for live-cell imaging of triads during myofiber contraction.
The complex interplays and trade-offs of live-cell imaging of triads during myofiber contraction can be illustrated through this Pyramid of Frustrations. One should aim to find a balance at the centre of the pyramid, at equal distance from the vertices. Adapted from Brameshuber (2022).

2. Objectives

With this project we aimed to elucidate the potential tethering relationship between triads and myofibrils, particularly at the A-I junction. To address it, we posed the following questions:

1) Do triads remain positioned at the A-I junction during sarcomeric length variation?

2) Based on triad positioning profile during contraction, which sarcomeric structure/proteins could potentially serve as anchors for triads?

For the technical objectives within this project, we intend to:

1) Establish a micropatterned *in vitro* system for the parallel alignment and individualisation of mature and contractile primary mouse skeletal myofibers.

2) Successfully implement a contraction stimulation approach for this *in vitro* system in order to induce synchronous myofiber contraction.

3) Achieve spatially and temporally resolved live-cell imaging of triads within a single sarcomere.

3. Material and Methods

3.1. Myoblast isolation and *in vitro* myofiber differentiation

All procedures using animals were approved by the Institutional ethics committee and followed the guidelines of the National Research Council Guide for the care and use of laboratory animals.

To achieve *in vitro* mature skeletal myofibers, we proceeded with the isolation, culturing and differentiation of primary mouse myoblast as previously published in Pimentel, *et al* (2017)[46]. From 5-7 days old C57BL/6 mice, tibialis anterior (TA), extensor digitorum longus (EDL), gastrocnemius (Gastro) and quadriceps muscles were dissected and kept in ice cold PBS. Muscles were digested mechanically using surgical scissors and incubated for 90 min at 37ºC with agitation in collagenase type V (Sigma Aldrich, St. Louis, MO) and dispase II (Invitrogen, Waltham, MA) in DPBS (Gibco, Carlsbad, CA). Digestion was stopped by adding dissection medium – 10% FBS, 1% Penicillin-Streptomycin (Thermo Fisher Scientific, Waltham, MA) in IMDM with Glutamax (Gibco). Cells in suspension were centrifuged for 5 min at 75 *g* to remove debris and adipose cells. Then, a second centrifugation step for 5 min at 350 *g* to pellet cells. These were resuspended in the same dissection medium and pre-plated for 4 hours at 37ºC and 5% CO_2, to allow for fibroblasts adherence. Afterwards, cells remaining in suspension were collected, centrifuged for 5 min at 350 *g* and resuspended in growth medium – 20% FBS, 1% Chicken Embryo Extract (made in house), 1% Penicillin-Streptomycin in IMDM with Glutamax. Plating was done either in patterned or unpatterned glass precoated with 1% or 10% Matrigel. Cell densities were kept between 250 000 – 220 000 and 200 000 – 180 000 cells/mL, respectively, and kept at 37ºC and 5% CO_2.

After 3 days of myoblast proliferation, cultures were changed to differentiation medium – 10% horse serum in IMDM with Glutamax – to induce myofiber maturation. On the following day, a topcoating of 50% Matrigel Matrix (Corning Inc., Corning, NY) in differentiation media was added and let to jellify for 30 min at 37°C. Differentiation medium was supplemented with 100 ng/mL of recombinant agrin (R&D Systems, Minneapolis, MN) and 100 ng/mL of fibroblast growth factor (FGF,

PeproTech, Waltham, MA). Half of the supplemented differentiation medium was changed every 2 days until imaging time-points, between 7-10 days post differentiation (D7-D10).

3.2. Deep-UV based micropatterning technique in glass coverslips

To keep skeletal myofibers unidirectionally aligned and individualised, we used an *in vitro* patterned system with a substrate topography of parallel linear regions of cell adhesion and non-adhesion. For this, we implemented and optimised a deep-UV based micropatterning technique described by Azioune, *et al* (2010) to achieve these linear regions[58].

First, borosilicate glass coverslips (#1.5H 25mm, Marienfeld, Lauda-Königshofen, Germany) were acid washed using 1M hydrochloric acid (VWR Chemicals Radnor, PA) for 5 min and rinsed multiple times with MilliQ water. Next, they were bathed in 95% ethanol, let to dry and stored in a sterile container. Micropatterning of washed coverslips was done at the day of primary myoblast culturing. We exposed coverslips to air plasma for 3 min, using a plasma cleaner (PDC-32G, Harrick Plasma, Ithaca, NY), for further cleaning and coverslip surface activation. Activated coverslips were coated with 0.1 mg/mL of pLL-g-PEG (4D cell, Montreuil, France) in 10 mM HEPES, pH 7.4 (Sigma Aldrich), for 30 min at RT protected from light. These were then washed in PBS to remove excess pLL-g-PEG and air dried for 2-3min, before placing them in the photomask for deep-UV micropatterning.

The 4Dcell quartz photomask with linear design (UM002, 4D cell) was used to micropattern parallel lines from 10 to 100 µm in width, distanced between each other from 50 to 120 µm. Photomask was thoroughly washed with detergent and distilled water, dried with kimwipes and cleaned with isopropanol (Merch KGaA, Darmstadt, Germany). Surface of the photomask was activated with 10 min exposure to deep-UV light inside an UV ozone oven (UVO-Cleaner, Jelight Company, Irvine, CA). Coverslips coated with pLL-g-PEG were carefully placed on the activated surface of the photomask, with their coated side in contact with the mask. For coverslips to adhere tightly, a drop of MilliQ water was added before coverslip placement. The

photomask was inserted inside the UV ozone oven at 5 cm from the lamp for 5 min. This forced the deep-UV light to travel only through the clear quartz regions of the photomask, removing the anti-adhesive properties of pLL-g-PEG in the designed linear regions. Coverslips were detached from the photomask using distilled water and washed three times with PBS. Sterilisation of coverslips was done by placing them under laminar flow cabinet's UV illumination for 5-10 min and kept sterile.

Next, we coated the UV-patterned linear regions with extracellular matrix (ECM) proteins by incubating the coverslips with 1% Matrigel in IMDM with Glutamax for 1h at RT. In an effort to enhance myofiber adhesion, alternative coating conditions were explored, including 10% Matrigel and a solution comprising 1% Matrigel and 2 µg/mL Fibronectin (F1141, Sigma Aldrich) in IMDM with Glutamax. No evident improvement in myofiber adhesion was seen, thus all further experiments were done with 1% Matrigel. In all situations, the patterned coverslips were washed one time with DPBS prior to the seeding of primary myoblast.

To evaluate the accuracy of pattern imprinting, coverslips were instead coated with 20µg/mL Fibronectin in 10mM HEPES (Sigma Aldrich), pH 7.4, and 7.5µg/mL Fibrinogen-Alexa Fluor 647 (F35200, Invitrogen) in PBS (Gibco), for fluorescence imaging. No myoblasts were seeded for these experiments.

3.3. Infection and transfection of plasmids. Fluorescent dyes incubation

For optogenetic induction of *in vitro* contraction with Channelrhodopsin-2, myofibers were infected with pACAGW-ChR2-Venus-AAV1 (Addgene viral prep # 20071-AAV1, Watertown, MA)[75] one day prior to the transition to differentiation medium. A solution of 1 µl of the viral preparation (1×10^{13} µg/mL) was added to 1 mL of growth medium and incubated with myofibers O/N at 37ºC with 5% CO_2. Cultures were washed once with PBS, before differentiation medium was added, as described above.

We exogenously expressed the following plasmids: α-Actinin-mCherry (Addgene plasmid #54975), α-Actinin-mCerulean (Addgene plasmid #55351), JPH1-iRFP, LifeAct-mNeonGreen (Addgene plasmid #98877)[76], LifeAct-miRFP703 (Addgene

plasmid #79993)[77], UtrCH-mNeonGreen (Addgene plasmid #98879)[76], UtrCH-mScarlet (Addgene plasmid #98823)[76]. The JPH1-iRFP plasmid was constructed by VectorBuilder. The vector ID is VB230104-1124suq, which can be used to retrieve detailed information about the vector on vectorbuilder.com. The plasmid coding sequence is CMV-XbaI-Kozak-iRFP670-3xGGGGS-HindIII-Junctophilin1-EcoRI, followed by a SV40 for transcription termination and polyadenylation, a pUC origin and an ampicillin cassette. Myofibers were transfected with the desired plasmid combination three days after culture, simultaneously with the switch to differentiation medium. For each plasmid, 1 µg was diluted in Opti-MEM (Invitrogen) and 2 µl of Lipofectamine 2000 (Invitrogen) also in Opti-MEM were carefully mixed, incubated for 10 min at RT and added to cultures in 1mL of differentiation medium. For previously infected cultures, medium was changed after 5 h, while for non-infected cultures, it was left O/N and then supplemented differentiation media was added. Topcoating and addition of supplemented differentiation medium were executed as described before.

To label F-actin, at imaging day cultures were incubated with 1 mM SiR-Actin dye (Spirochrome, Stein a.R., Switzerland) for 1 h, washed once with DPBS and then incubated with the membrane dye CellMask Orange 5 µg/mL (Invitrogen) for 30-45 min. One final wash with DPBS was done and imaging was carried out using supplemented differentiation medium.

3.4. Immunofluorescence microscopy of *in vitro* myofibers

In vitro myofibers were fixed at time-points of interest (between D7-D10) with 4% paraformaldehyde (PFA, Electron Microscopy Sciences, Hatfield, PA) for 10 min at RT. Next, they were rinsed twice in PBS for 1 min and permeabilized with 0.5% Triton X-100 (Sigma Aldrich) diluted in PBS for 5 min at RT. Myofibers were washed again with PBS and incubated with blocking solution – 5% bovine serum albumin (BSA, Sigma Aldrich), 10% goat serum (GS, Sigma Aldrich) in PBS – for 30-60 min at RT. Afterwards, primary antibodies were diluted in blocking solution supplemented with 0.1% saponin (Sigma Aldrich) and incubated O/N at 4ºC. The following day, myofibers were washed three times in PBS for 5 min with gentle agitation. Secondary

antibodies and DAPI (1:10 000, Sigma Aldrich) were diluted in 0.1% saponin blocking solution and incubated for 30-60 min at RT. Finally, myofibers were washed with PBS and covered with Fluoromount-G (Invitrogen). Primary antibodies included mouse monoclonal anti-sarcomeric-α-Actinin (1:200, Sigma Aldrich), rabbit polyclonal anti-α-Actinin (1:200, Thermo Fisher Scientific), rabbit polyclonal anti-JPH1 (1:200, Invitrogen), mouse monoclonal anti-TMOD1 (1:200, Invitrogen). Secondary antibodies included Alexa Fluor 488–conjugated goat anti-mouse and rabbit IgG (1:400, Invitrogen), Alexa Fluor 555–conjugated goat anti-mouse and rabbit IgG (1:400, Invitrogen). Far red SiR-Actin dye (1:1000) was used to stain F-actin.

Wide-field immunofluorescence images of the *in vitro* patterned system and aligned mature myofibers were captured with a Zeiss Cell Observer SD inverted microscope using a 10x EC Plan-Neofluar Ph1 (NA=0.3) or 20x Plan-Apochromat Ph2 (NA=0.80) objective. Digital images were acquired by sCMOS camera Hamamatsu ORCA-flash4.0 V2. Confocal point-scanning imaging was performed with Zeiss LSM 980 Airyscan2 inverted microscope using a 63x Plan-Apochromat DIC Oil objective (NA=1.40).

3.5. High-speed live-cell imaging of *in vitro* myofibers

For high-speed live-cell acquisition of myofiber contraction we used a Zeiss LSM 980 Airyscan 2 point-scanning confocal inverted microscope equipped with a GaAsP detector, a 37ºC and 5% CO_2 chamber and a piezo controlled stage. For the initial assessment of Sarcomeric Lenght (SL) variation, a single channel was imaged using the LSM980 Multiplex SR-4Y with 63x Plan-Apochromat DIC Oil objective (NA=1.40), which achieved 10 ms/frame (100Hz) acquisition time. For simultaneous imaging of triads and sarcomeric actin, the same single channel imaging setup was tested, now with both 561 nm and 639 nm excitation lasers activated. However, due to the close proximity between the cellular structures of interest, we transitioned to Multiplex SR-4Y dual-channel imaging with line wise switching, which provided an acquisition time of 13-14 ms/frame (71-77 Hz). All images acquired were reconstructed with the ZenBlue software using automatic noise filters.

For brightfield imaging of electrically induced myofiber contraction, Nikon Eclipse Ti inverted microscope was used with a 40x CFI S Plan Fluor ELWD ADM Ph2 objective (NA=0.60) and a MyoCam-S3 camera. Exposure time was set to 10 ms.

3.6. Optogenetic approach for stimulation of myofiber contraction

We tested approaches of photo-stimulation using a light source external to the microscope's illumination system: placement of blue light optical fibre in culture medium above myofibers; positioning of 4 blue LED's focused on the central region of the coverslip. Unfortunately, both approaches proved ineffective in inducing myofiber contraction. We believe that the scattering of light in culture medium lead to the non-uniform distribution of light, and insufficient stimulation of myofibers.

Therefore, we adopted ON/OFF modulation of the Zeiss LSM 980 microscope's illumination system to induce myofiber contraction. Activation of blue 475 nm LED illuminated a substantial area of the coverslip, resulting in observable contraction of ChR2-Venus expressing myofibers. However, using this LED for the experimental design was not possible due to its light path incompatibility with image acquisition.

Using the Experimental Design tool in ZEN Blue Software, we configured a filterset that allowed the simultaneous excitation of 488 nm, 561 nm and 639 nm lasers, while only capturing the emission spectrum from stained structures of interest (580-759 nm). This configuration enabled the selective activation/deactivation of the blue (488 nm) laser for myofiber stimulation, without capturing its emission spectrum or delaying time acquisition. The tested power of the blue laser ranged from 0.26–1.3 mW. At the higher end of this power range, myofibers tended to collapse from 488 nm activation, frequently after fluorescent dyes incubation. Nonetheless, out of a comprehensive number of imaged myofibers, few reacted to 488 nm laser stimulation. We attributed this to a reduced field of view, necessary for high-speed imaging, which limited the myofiber area illuminated by the laser. Consequently, photo-activation of ChR2 occurred in an insufficient number of cells to robustly induce myofiber contraction.

3.7. Electrical field stimulation approach to myofiber contraction

To confirm the modulation capacity of electrical field stimulation in myofiber contraction, we used the Ionoptix *in vitro* stimulation system (Myopacer, Ionoptix, Amsterdam, The Netherlands). We experimented with electrical pulses at varying voltages, including 4V, 6V and 10V, at frequencies of 0.5Hz or 1Hz. Also, pulse durations of 4 ms, 50 ms and 500 ms were tested. For measurements related to triad distance variation, a consistent electrical pulse of 6V at 1Hz for 500 ms was employed after 2 sec imaging of myofiber at resting state.

To couple electrical field stimulation to the patterned *in vitro* system, a homemade electrical field stimulation setup was made inspired by the already established Myopacer setup. We coupled a monophasic electrical stimulator (S48, Grass Instrument Division, West Warwick, RI) to a photoelectric stimulus isolation unit (PSIU6, Grass Instrument Division) which reduces stimulus artefacts and minimises effects of electrode capacitance. These were connected to two tinned copper electrodes positioned 15mm apart in parallel and less than 1mm above myofibers, submerged in culture medium. Electrodes were attached to the lid of the 35mm culture dish (World Precision Instruments, Sarasota, FL) and integrated into our coverslip imaging chamber (Chamlide CMB, Live Cell Instruments, Gyeonggi-do, Republic of Korea).

3.8. Whole muscle isolation and contraction/stretching experimental procedures

TA muscles were extracted from C57BL/6 mice aged 4-6 months, maintaining the tendons attached to the tibia bone. Dissected muscles were kept in Ringer's solution containing (mM): 140 NaCl (Sigma-Aldrich), 5 KCl (Sigma-Aldrich), 3.2 $CaCl_2$ (Sigma-Aldrich), 1.1 $MgCl_2$ (Sigma-Aldrich), 1.1 Na_2HPO_4 (Sigma-Aldrich), 0.4 NaH_2PO_4 (Sigma-Aldrich) (pH 7.4), 4.5 glucose (Sigma-Aldrich) at 37ºC with aeration.

For stretching conditions, 1 µg/mL *d*-Tubocurarine chloride (d-TC, Sigma-Aldrich) was added to Ringer's solution. After 15 min incubation, the muscles were manually

stretched until their length increased by 1, 2 or 3 mm. To induce contraction, muscles underwent incubation with varying concentrations of potassium chloride (KCl, Sigma-Aldrich) - specifically, 100 nM, 140 nM, and 180 nM - for a duration of 15 minutes.

3.9. Whole muscle preparation for cryosectioning

All stretched, contracted and control muscles were pre-fixed in 2% PFA in Ringer's solution for 3 h at 4ºC and washed three times with PBS for 10 min. Cryopreservation of muscle tissue was done with increasing concentrations of sucrose (Thermo Fisher Scientific) from 15% up to 30% diluted in MilliQ water, for 16 h at 4ºC. Muscles were rapidly frozen in 2-methylbutane (VWR Chemicals) cooled in liquid nitrogen for 30-40 sec. Samples were stored at -80°C until cryosectioning.

Cryosections of 8 µm thickness from TA muscles were performed longitudinally, focusing on the peripheral region of the muscle, since KCl penetration may not reach the centre of the muscle. Thus, the peripheral region of the tissue is the most influenced by KCl. These sections were stored at -80°C.

3.10. Whole muscle immunofluorescence microscopy

Prior to immunofluorescence and to restore epitope-antibody reactivity, muscles were subjected to low pH heat-induced epitope retrieval (HIER) standard protocol using PT Link Module (Agilent, Santa Clara, CA), which maintained tissue sections at 100ºC for 1 h. Afterwards, sections were washed for 10 min in 0.1% Tween-20 detergent (Sigma-Aldrich) diluted in PBS (PBST). Blocking solution – 5% BSA, 30µg/mL VisUBlock Mouse on Mouse Blocking Reagent (R&D Systems, Minneapolis, MN), 0.1% Triton X-100 in PBS – was incubated for 2 h at RT. Primary antibodies were diluted in antibody solution – 2% BSA, 5% Goat Serum, 0.1% Triton X-100 in PBS – and incubated O/N in a wet chamber at 4ºC. The following day, muscle sections were rinsed four times with PBS with 0.1% Tween-20 (PBS-T) for 10 min and incubated with secondary antibodies diluted in previously described antibody solution and DAPI (1:10 000) for 2 h 30 min at RT in a wet chamber. Finally, sections were washed five times with PBS-T and slides mounted with Fluoromount-

G. Primary antibodies included mouse monoclonal anti-sarcomeric-α-Actinin (1:200, Sigma Aldrich) and rabbit polyclonal anti-JPH1 (1:200, Invitrogen). Secondary antibodies included Alexa Fluor 488–conjugated goat anti-rabbit IgG (1:400, Invitrogen) and Alexa Fluor 555–conjugated goat anti-mouse IgG (1:400, Invitrogen).

Super-resolution confocal point-scanning imaging was performed with the Zeiss LSM 980 using Airyscan2 with 63x Plan-Apochromat DIC Oil objective (NA=1.40).

3.11. Image analysis and quantifications

All images were processed in Fiji 1.54 (Schindelin et al., 2012)[78]. Myofiber maturation in the patterned *in vitro* system was analysed based on three hallmarks of myofiber differentiation – Z-line transversal alignment, peripheral nuclei, and triads transversal organisation[79]. For mature myofiber quantification, we considered only myofibers exhibiting both α-Actinin and JPH1 transversally aligned, along with DAPI staining at the periphery.

For SL quantifications, only myofibers with transversal alignment of sarcomeres were selected. From these, fluorescence plot profiles were generated by drawing a line perpendicular to transversal sarcomere orientation. SL measurements were derived by subtracting the X-values of adjacent fluorescence peaks on these plots. In myofibers expressing α-Actinin-mCherry or immunostained with α-Actinin antibodies, fluorescence peaks indicated the positioning of Z-lines. Thus, SL values were obtained from distance between Z-lines. Conversely, in myofibers labelled with SiR-Actin the highest intensity fluorescence peaks corresponded to the pointed-ends of F-actin, near the M-band. Note that, at resting state, myofibers occasionally exhibited a single peak per sarcomere, while in other cases, two peaks were observed. In instances with dual peaks, the middle distance between them served as the reference for subsequent quantification. Thus, in myofibers labelled with SiR-Actin, SL values represent the distance between M-bands.

For quantification of distance between triads (DT), myofibers with transversal T-tubules/triads were considered. The same analysis method was employed to calculate the distance between adjacent highest intensity fluorescence peaks from myofibers labelled with CellMask or immunostained for JPH1. We subdivided DT

measurement into two categories: the distance between triads over the M-band (DT-M), representing the distance between triads of the same sarcomere, and the distance between triads over the Z-line (DT-Z), representing the distance between consecutive triads from adjacent sarcomeres.

From live imaging acquisitions, we extracted SL, DT-M and DT-Z values at a given resting time-point and, following myofiber stimulation, at peak contraction and/or stretch. Using GraphPad Prism (San Diego, CA), we generated violin plots of the distribution of SL measurements from contracting (n=5 sarcomeres), resting (n=22) and stretching (n=22) myofibers. Then, SL values from 14 sarcomeres at each myofiber state were plotted with the respective DT-M and DT-Z. To understand single sarcomere variation of these measurements, we highlight within the graph the values observed from resting state to contraction and from resting to stretching of two example myofibers. Arrows used for this purpose originate in resting values and point towards values post-myofiber stimulation.

Similarly, the distribution of SL measurements from whole muscles contracted with 180mM, 140mM or 100mM KCl, in control conditions and stretched 1 or 2mm, were graphed in violin plots, with each condition having n=40-60 sarcomeres. For correlation analysis between SL and DT-M / DT-Z, we plotted values obtained from myofibers contracted with 180 or 140mM KCl, stretched 2mm and in control conditions, totalling 83-93 sarcomeres from 10 distinct myofibers per sarcomeric state.

3.12. Statistical analysis

All graphs and statistical tests were performed with GraphPad Prism. Statistical significance is represented as follows: **** $p < 0.0001$; *** $p < 0.001$; ** $p < 0.01$; * $p < 0.05$, ns no significance. In live myofiber imaging, we compared SL values distribution from contracting and stretching myofibers with their initial value at resting state, using a Wilcoxon matched pairs signed rank test. In fixed whole muscle, SL distribution per experimental condition was compared to control muscles through Mann-Whitney statistical tests. To study the correlation between SL and DT-M / DT-

Z, from both *in vitro* and *ex vivo* results, we performed Spearman correlation tests and graphed best-fit lines for each group, for which linear correlation was assumed.

4. Results

4.1. Patterned *in vitro* myofibers results in unidirectional alignment of mature skeletal myofibers.

For effective single-sarcomere imaging during myofiber contraction, it is helpful to ensure that myofibers are unidirectionally aligned and remain individualised. Avoiding myofiber overlap can prevent undesirable cell displacement during contraction imaging. Thus, we implemented and optimised a substrate micropatterning protocol using deep-UV light and glass coverslips. With this quick and affordable technique, we created specific regions of cell adhesion and non-adhesion, forcing cell adherence and growth within a given pattern. For the intended myofiber positioning, we used a commercially available quartz photomask with parallel lines pattern (UM002, 4Dcell, France), where line width varied from 10 to 100 µm and space in between lines from 50 to 120 µm. To produce the non-adhesion regions, we used pLL-g-PEG polymer after passivating the glass coverslip surface. To validate the correct imprinting and sharpness of the pattern, we fluorescently labelled adhesion regions by coating them with fibronectin and fibrinogen-AF488 (Figure 7A). For all other experiments, we coated the adhesion regions with 1% Matrigel Matrix typically used for myoblast attachment and differentiation.

We followed previously established protocols for isolation and proliferation of primary mouse myoblasts, as well as differentiation to achieve mature skeletal myofibers after 7-10 days post differentiation (D7-D10)[46].

Parallel alignment of myofibers in the patterned glass coverslips was successful, although some myofibers can be seen escaping the linear adhesion regions (Figure 7B). This can probably be attributed to pLL-g-PEG degradation which is known to occur with long-term cell cultures[80]. To achieve mature myofibers (i.e. with transversal triads) requires at least 10 days in culture. Therefore, using other non-adhesive polymers more resistant to chemical degradation in long-term culture, such

as pLL-g-PMOXA, should be considered in the future[80]. Various degrees of myofiber individualisation were also observed, varying with myoblast seeding density and pattern region location (given the different pattern line widths). Notably, regions with more individualised myofibers resulted in less differentiation. Previous research using primary myoblast cultures has indicated that, at low cellular densities, myoblast proliferation is stimulated while differentiation is inhibited[81]. Despite this, we identified regions where myofibers were aligned and more individualised, which facilitated further imaging of subcellular structures during contraction.

Next we assessed the following maturation hallmarks: Z-line transversal alignment, confirmed using **α**-Actinin staining; peripheral nuclei with DAPI; and triad organisation with transversal JPH1 staining (Figure 7C). Overall, myofiber maturation was not majorly affected by culture in patterned glass coverslips. Obtained percentages of myofibers with transversal JPH1 – representing triad transversal alignment, the final hallmark of myofiber maturation – were 38% and 45% at D7 and D10, respectively, compared to 56% and 46% in unpatterned glass at these same time-points (Figure 7D). During time in culture spontaneous contractions could be seen in both patterned and unpatterned *in vitro* systems. This suggested that myofibers were functional.

4.2. High-speed imaging of contracting skeletal myofibers.

To capture skeletal myofiber contraction was essential to maintain a frame acquisition time below 20-10 ms, the estimated time of contraction response after nervous stimulus *in vivo*[66,67]. Moreover, assuring super-resolution is crucial for accurate localisation of triad positioning within the sarcomere. We therefore employed the high-speed super resolution Zeiss LSM 980 Airyscan SR-4Y microscope. For contraction stimulation, we experimented with two distinct approaches: optogenetic and electrical field stimulation (see below).

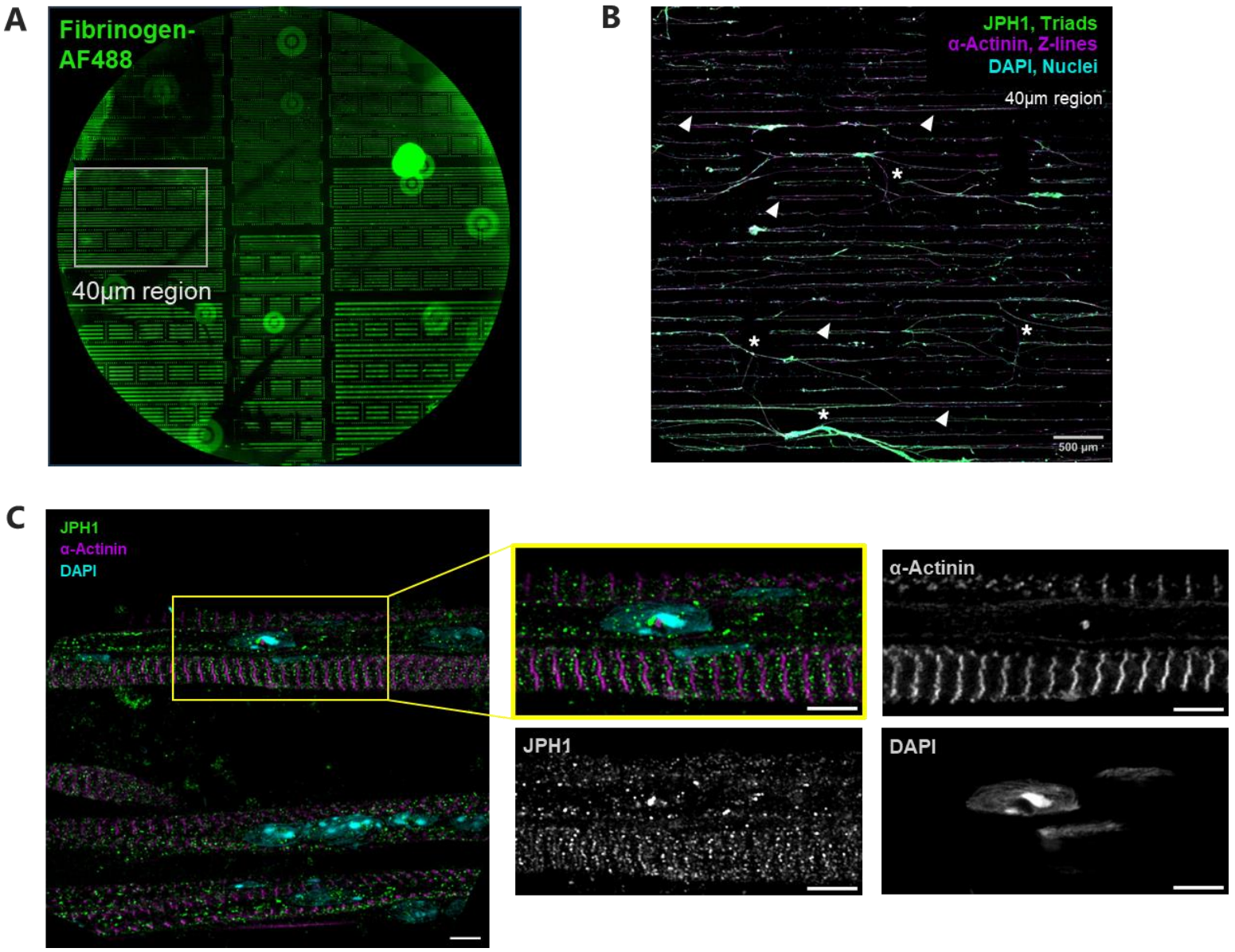

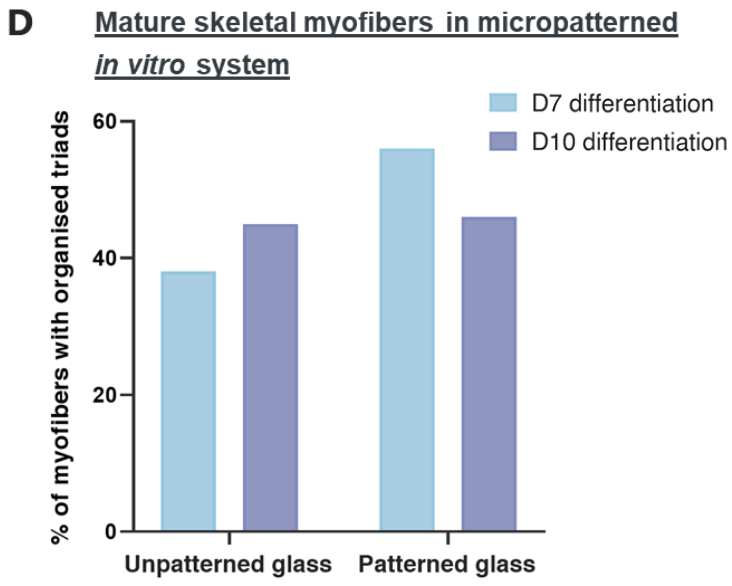

Figure 7. Myofibers cultured in our micropatterned in vitro system align longitudinally, become more isolated and fully mature.

A. Assessment of correct imprinting of the linear pattern after UV micropatterning technique. Glass coverslip coated with fibronectin and labelled with fibrinogen-AF488. **B.** Representative immunostaining of primary mouse myofibers in patterned glass coverslips at day 10 of differentiation (D10) showing myofiber alignment. Arrowheads point at parallel aligned myofibers, and asterisks denote regions where myofibers escape pattern's linear adhesion regions. **C.** Representative myofiber from patterned glass showing all hallmarks of maturation - sarcomere alignment (transversal Z-lines), peripheral nuclei and transversal triads. Antibodies anti-α-Actinin used as Z-line marker, anti-JPH1 as triad marker and DAPI used for nuclei staining. Scale bar 5 µm. **D.** Percentage of mature myofibers in patterned versus unpatterned glass by counting cells displaying transversally aligned JPH1 (n=50 myofibers for unpatterned D7/D10 and patterned D10; n=20 patterned D7).

4.2.1. Actin and triad labelling probes for live-cell imaging.

Tracking triad positioning during myofiber contraction raises the necessity of labelling not only the triads, but also sarcomeric structures that delineate and highlight single-sarcomere length variation. In fixed cells, fluorescent Phalloidin has been shown to label F-actin and accumulate at the Z-lines[117]. However, Phalloidin is not compatible with live cell imaging. Therefore, we started by testing several live-cell actin probes. For this we transfected *in vitro* myofibers with LifeAct-mNeonGreen, LifeAct-miRFP703, UtrCH-mNeonGreen or UtrCH-mScarlet. These are actin binding domains that have been previously described to label F-actin. In our primary skeletal myofibers utrophin (UtrCH) concentrated at the Z-lines. Interestingly, when using the LifeAct probe, containing the same actin binding domain sequence but with different fluorescent proteins – mNeonGreen or miRFP703 – its localisation changed from the Z-line to the M-band region (Figure 8A).

Additionally, we also tested the transfection of α-Actinin-mCherry in *in vitro* myofibers, which fluorescently labelled sarcomeric Z-lines with a stronger fluorescent intensity than the probes tested above (data not shown). For triad labelling, myofibers were transfected with the SR protein Junctophilin 1 (JPH1-iRFP) (Figure 8B). Unfortunately, transfecting myofibers led to increased cell death, which became particularly evident in the patterned system. Increasing cell density did slightly help raise the pool of mature myofibers and some with striated α-Actinin-mCherry labelling were found. The JPH1 transversal alignment could also be seen, although the signal was noisy. We proceeded with our experimental design and assessed these myofibers' contractility. We realised that α-Actinin-mCherry would rapidly photobleach (Figure 8C) since our high-speed imaging setup requires about 200 images to be acquired.

Altogether, transfecting cells in the micropatterned system yielded a small number of myofibers with striated α-Actinin-mCherry labelling and this fluorescent protein rapidly photobleached during the high-speed imaging. Therefore, we turned our

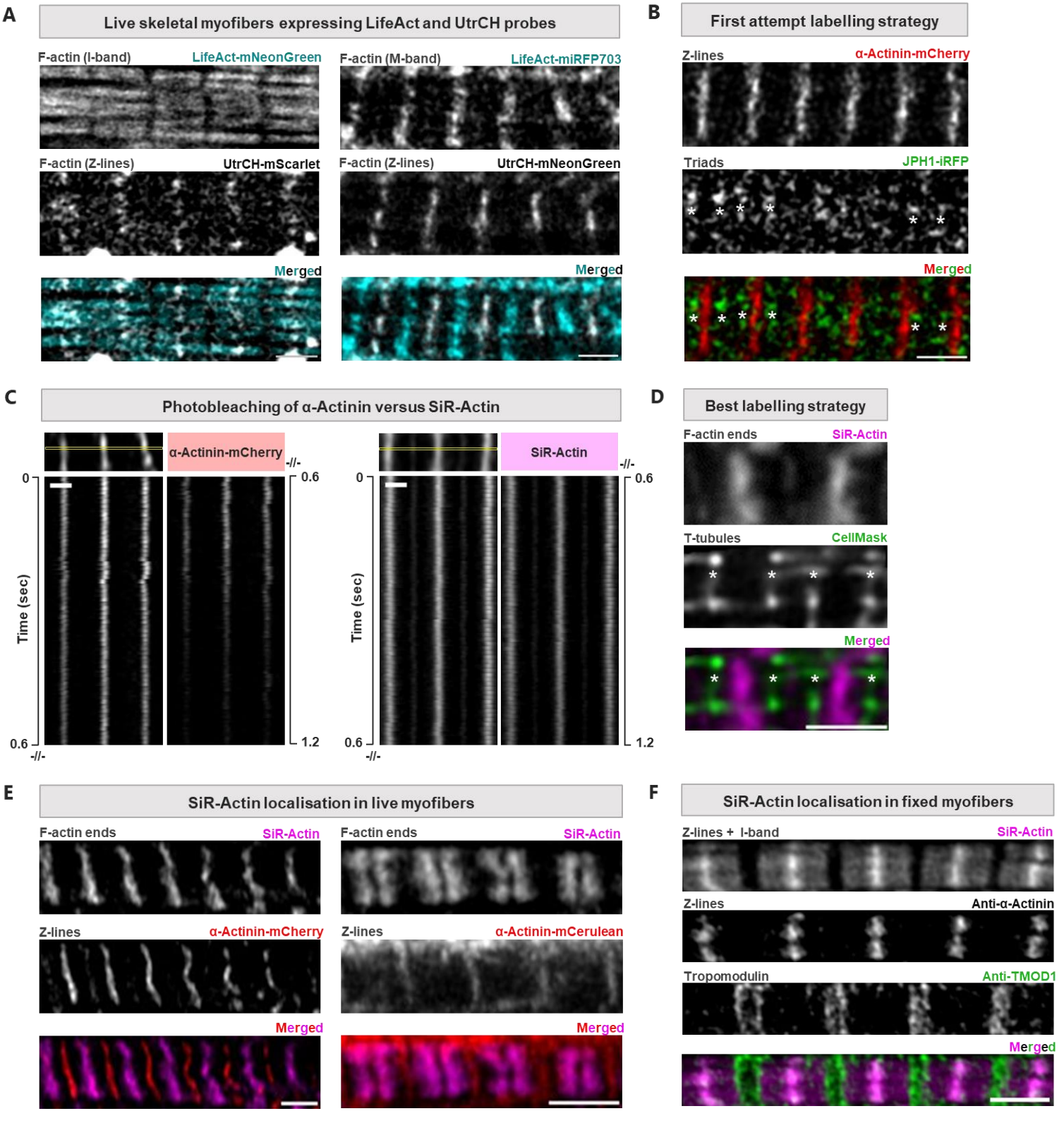
A
Live skeletal myofibers expressing LifeAct and UtrCH probes
F-actin (I-band)
LifeAct-mNeonGreen
F-actin (M-band)
LifeAct-miRFP703
F-actin (Z-lines)
UtrCH-mScarlet
F-actin (Z-lines)
UtrCH-mNeonGreen
Merged
Merged
B
First attempt labelling strategy
Z-lines
α-Actinin-mCherry
Triads
JPH1-iRFP
Merged
C
Photobleaching of α-Actinin versus SiR-Actin
α-Actinin-mCherry
SiR-Actin
Time (sec)
0
0.6
1.2
-//-
D
Best labelling strategy
F-actin ends
SiR-Actin
T-tubules
CellMask
Merged
E
SiR-Actin localisation in live myofibers
F-actin ends
SiR-Actin
Z-lines
α-Actinin-mCherry
α-Actinin-mCerulean
Merged
F
SiR-Actin localisation in fixed myofibers
Z-lines + I-band
SiR-Actin
Z-lines
Anti-α-Actinin
Tropomodulin
Anti-TMOD1
Merged

Figure 8. SiR-Actin and CellMask fluorescent dyes are the best available labelling strategy for live-cell imaging of sarcomeres and triads.

A. Representative images of LifeAct and UtrCH F-actin probes in live primary skeletal myofibers. Left myofibers expresses LifeAct-mNeonGreen (cyan, binds to the I-band) and UtrCH-mScarlet (gray, binds to Z-lines). Right myofiber expresses LifeAct-miRFP703 (cyan, binds to M-band) and UtrCH-mNeonGreen (gray, once again binds to Z-lines). **B.** Localisation of α-Actinin-mCherry and JPH1-iRFP in in vitro skeletal myofibers. α-Actinin binds to the Z-lines as expected. JPH1-iRFP labelling appears noisy, and it was rare to find myofibers expressing it. Asterisks locate triads. **C.** Fluorescence imaging highlighting the higher photobleaching resistance of SiR-Actin compared to α-Actinin-mCherry in live myofibers. Kymographs of each myofiber over 1.2 seconds of high-speed super-resolution imaging. **D.** Myofiber labelled with fluorescent dyes SiR-Actin (magenta) and CellMask (green), showing good T-tubule alignment and good intensity labelling with both dyes. Asterisks highlight T-tubules. **E.** Assessing SiR-Actin's (magenta) sarcomeric binding region through co-localisation with α-Actinin-mCherry (red) in live myofibers. No co-localisation was observed, leading to believe that SiR-Actin is binding to the pointed-ends of thin filaments (F-actin ends). **F.** Confirmation of SiR-Actin (magenta) binding close to the terminal region of thin filaments by co-localisation with TMOD1 (green) and α-Actinin (gray) through immunofluorescence of fixed in vitro cultures. Notice that SiR-Actin staining changes fluorescence profile after myofiber fixation, changing its affinity from F-actin ends to the Z-lines and spreading through the I-band. All scale bars 2 μm.

attention to cell-permeable fluorescent dyes, which would avoid interference with myofiber maturation and be more resistant to photobleaching.

We tested SiR-Actin, a jasplakinolide-derived F-actin dye, which has been shown to label with highest intensity at the Z-line region in live isolated mouse EDL myofibers[82]. In our experiments, live-cell imaging of SiR-Actin labelled myofibers revealed a higher intensity region seemingly close to the ends of thin filaments (F-actin ends) and a fainter line possibly at the Z-line (Figure 8D). This fluorescence pattern has also been seen in live isolated mouse FDB myofibers with SPY555-FastActin labelling – another jasplakinolide-derived F-actin dye[83].

We hypothesised that SiR-Actin was preferentially binding to a region close to the M-band. To test this, we expressed α-Actinin to label the Z-lines and incubated those myofibers with SiR-Actin. We observed no co-localisation, with SiR-Actin signal aligning halfway the distance between two Z-lines. Additionally, we noted that distinct myofibers displaying similar SL could present a single-line profile for SiR-Actin, while others exhibited two lines, as seen in example myofibers from Figure 8E. This suggested that SiR-Actin was binding at a region close to the M-band. In order to confirm that SiR-Actin staining could be accumulating at the end region of thin filaments, we co-immunostained fixed myofibers with SiR-Actin dye, tropomodulin

(TMOD) and α-Actinin antibodies. Interestingly, in fixed myofibers the whole I-band was stained by SiR-Actin dye, with the highest intensity region shifting to the Z-lines – co-localising with α-Actinin. TMOD delineated these I-band regions (Figure 8F), suggesting that indeed the highest intensity region in live-cell SiR-Actin labelling could refer to F-actin at the pointed ends of thin filaments.

As expected, SiR-Actin photobleaching was lower than the α-Actinin-mCherry fluorescent protein (Figure 8C). Its cell-permeability also allowed for myofibers to mature undisturbed in the patterned coverslips until imaging time-point, since no transfection of cultures was required. Hence, we proceeded with SiR-Actin labelling for further experiments, using the F-actin ends region as reference for SL measurements.

For triad labelling, we opted for CellMask Orange fluorescent dye which generally labels plasma membrane (Figure 8D). Considering that T-tubules are invaginations of the plasma membrane and an integral component of triads, we used their localisation as reference of triad positioning[84,85].

4.2.2. Optogenetic approach failed to induce myofiber contraction in our system.

In parallel, we began to implement an optogenetic approach to stimulate contraction in our *in vitro* skeletal myofibers. This technique allows for the induction of myofiber contraction through photo-stimulation. First, we expressed Channelrhodopsin-2 (ChR2)-Venus, a type of light-activated cation channel which depolarizes the plasma membrane after blue light (488 nm) stimulation, leading to myofiber contraction. For ChR2-Venus genetic construct delivery, we used AAV1 viral vector and infected our cultures at a time-point before differentiation[75]. At the start of differentiation, we transfected *in vitro* myofibers with our α-Actinin-mCherry fluorescent probe to mark the sarcomeric Z-line. With this optogenetic approach, we obtained myofibers expressing both ChR2 and α-Actinin (Figure 9A), allowing further study of myofibers' contractility after photo-stimulation. Overall, in patterned glass we obtained a high proportion of myofibers that were successfully transduced with ChR2. Approximately half of ChR2 expressing myofibers were also expressing α-Actinin (Figure 9A).

However, few transfected myofibers had transversally organised α-Actinin, meaning that infection and/or transfection steps were hindering myofiber maturation. By changing our sarcomere labelling approach towards SiR-Actin fluorescent dye, we observed a higher number of myofibers expressing aligned sarcomeres with transversal Z-lines, even after AAV1-ChR2-Venus infection (data not shown).

Ideally, photo-stimulation of myofibers' contraction would be given by an external blue LED placed over the *in vitro* system, with programmable intensity and pulse frequency. We tested two techniques further described in the *Material and Methods* section, but no contractions were detected when blue light was activated from external sources. We hypothesise that the light is scattered within the culture medium, not reaching myofibers uniformly or with enough intensity to activate ChR2. Therefore, we opted for ON/OFF modulation of ZEISS LSM 980 microscope's 488 nm laser.

During live myofiber imaging, our optogenetic contraction stimulation plan began with 1 sec of 488 nm laser OFF followed by 1 sec laser ON. Using Multiplex SR-4Y mode in ZEISS LSM 980 we could obtain 10 ms of acquisition time with a theoretical axial resolution of 140 nm. We also tried to image by iSIM but the signal-to-noise was too low. Both in patterned and unpatterned glass we detected three types of myofiber response to photo-stimulation. Altogether, 36 imaged myofibers did not react to the stimulus, 5 showed partial induced contractions and 15 had complete induced contractions. We studied kymographs of cells that produced complete or partial induced contractions following photo-stimulation (Figure 9C) and compared them to kymographs of spontaneously contracting cells (Figure 9B). Kymographs visually depict changes in the positioning of labelled structures over time, with time represented on the vertical axis and spatial position on the horizontal axis. Notably, we observed that photo-stimulated contractions occurred more rapidly, manifesting within a few frames, whereas spontaneous contractions exhibited a more prolonged duration. In conclusion, employing this optogenetic approach resulted in a limited number of contracting myofibers after photo-stimulation. When contractions

occurred, our observations lacked the temporal resolution needed to track the motion of labelled structures.

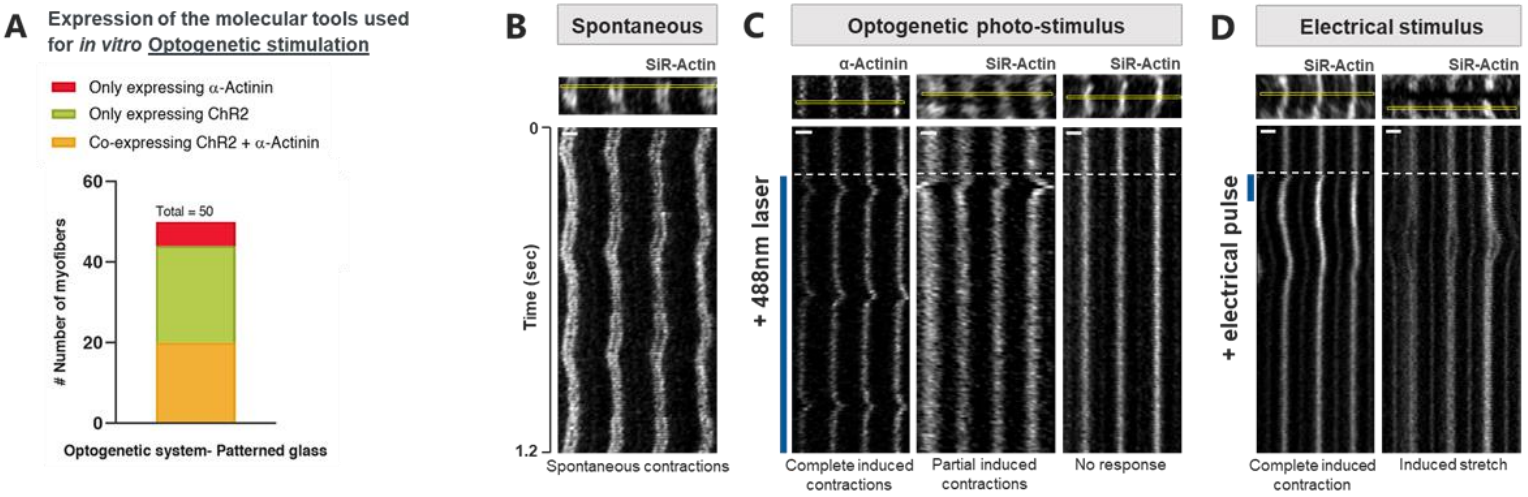

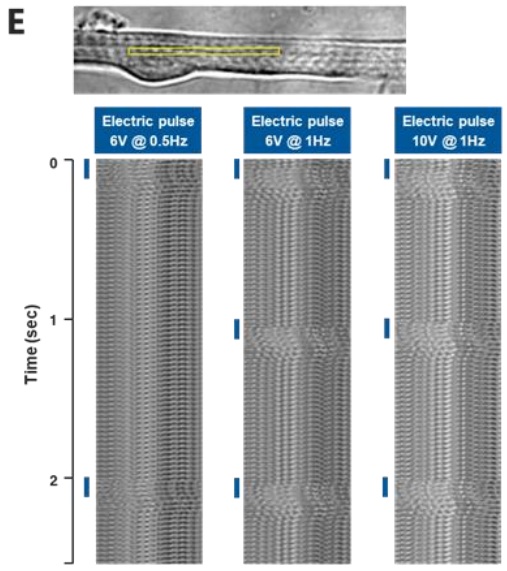

Figure 9. Single-sarcomere imaging of contracting myofibers detected both shortening and lengthening of sarcomeres after electrical field stimulation. Optogenetic stimulation did not efficiently induce myofiber contraction in our in vitro system.

A. Quantification of absolute number of myofibers that express only one or both genetic constructs used in optogenetic stimulation approach, AAV1-ChR2-Venus and α-Actinin-mCherry (n=50, N=1). **B-D.** Representative kymographs from six different myofibers showing sarcomeric length variations during contraction. **B**. Example of myofiber spontaneously contracting and displaying sarcomere shortening followed by a quick return to resting state. **C.** Example myofibers show differential response to optogenetic stimulation of contraction. From left to right, myofiber displays complete induced contraction, with sarcomere shortening; partial induced contraction with one-time sarcomere shortening; no myofiber response to the electrical stimulus was detected. **D.** Example myofibers after electrical field stimulation. In some myofibers sarcomeres shorten (left), others stretch (right). Scale bars 1µm. **E.** Brightfield image of a single live myofiber in vitro. Kymographs from brightfield imaging of this single myofiber highlight contraction modulation capacity gained from electrical field stimulation. Electrical pulses given were 6V 0.5Hz, 6V 1Hz and 10V 1Hz, from left to right.

4.2.3. Electrical field stimulation induces both myofiber contraction and stretching.

To modulate contraction in *in vitro* myofibers, we explored an alternative stimulation approach - electrical field stimulation. By varying voltage and frequency of the electrical stimulus, we could alter myofiber contraction *in vitro*. We analysed the kymographs derived from brightfield imaging of the same myofiber subjected to three electrical stimuli: 6V at 0.5Hz, 6V at 1Hz and 10V at 1Hz, all for 4 ms pulse duration (Figure 9E). Our findings validated that *in vitro* myofibers contracted according to stimulus frequency and that increasing voltage did not significantly change contraction profile. For the remainder of our experiments an electrical stimulus of 6V at 1Hz was used.

Enhanced temporal resolution was achieved using electrical field stimulation, as evidenced by the kymograph of myofiber displaying a more prolonged complete induced contraction (Figure 9D) than obtained previously with photo-stimulation. This allowed us to proceed with the quantification of the SLs derived from *in vitro* myofibers subjected to electrical stimulation. Ideally, SL would be measured from Z-line to Z-line, but SiR-Actin labelling was too faint within these lines to allow the accurate measurement of this distance. Therefore, we measured the distance between F-actin ends from adjacent sarcomeres as reference to determine myofibers' SL (Figure 10A).

During experimental work, spontaneously contracting myofibers were captured and kymographs revealed sarcomere shortening with a quick return to resting state (Figure 9B). Interestingly, electrically stimulated sarcomeres tended to increase their SL above their resting values, in a stretching motion. In some cases, this stretching was followed by contraction, resulting in a SL lower than observed during resting state (Figure 9D, *Complete induced contraction*). In most myofibers only stretching was observed (Figure 9D, *Induced stretch*).

Next to test if our SL variations are significant in resting versus stimulated conditions, we used the Wilcoxon matched pairs signed rank test, and saw that during stretching

each individual sarcomere was statistically different from its initial resting SL ($p<0.0001$). However, the SL shortening seen in contracting sarcomeres was not significantly different from its initial resting SL. Despite the lack of statistical significance in contracting values, it is pertinent to highlight that all SL variation measured in contracting myofibers exceeded our microscopy resolution theoretical limit of 140 nm. This reinforced our confidence in attributing the observed sarcomere shortening to a physiological contraction rather than artefacts.

Overall, at resting state myofibers had on average a SL of 2.33 µm. After electrical stimulation, we recorded an average of 2.08 µm for SL in contracting myofibers, which represents a sarcomeric shortening of 11%. In stretching myofibers the average reached 2.91 µm representing a sarcomeric stretching of 25% (Figure 10B).

4.3. Asymmetry in the dynamics of triad distance within and between sarcomeres during sarcomeric length variation.

To investigate triads positioning at the A-I junction during sarcomeric movement, myofibers were labelled with both SiR-Actin and CellMask fluorescent dyes. For each myofiber, we quantified the distance between triads and the respective SL during resting state, as well as at the peak of contraction and/or stretching, following electrical field stimulation.

Regarding distance between triads (DT), we subdivided this measurement into two categories: the distance between triads flanking the M-band (DT-M), representing the distance between triads of the same sarcomere, and the distance between triads flanking the Z-line (DT-Z), representing the distance between consecutive triads from adjacent sarcomeres (Figure 10A). According to our initial hypothesis, if triads are anchored to the myofibrils at the A-I junction, then the values of DT-M should remain relatively constant despite sarcomeric movement. In other words, the DT from the same sarcomere should not correlate with sarcomere movement during contraction and stretching (Figure 5).

Altogether, SL and DT measurements were collected from 14 sarcomeres across four distinct batches of myofiber cultures. Plot profiles from contracting myofibers showed triads from the same sarcomere moving slightly closer together towards the M-band compared to consecutive triads from adjacent sarcomeres (Figure 10C, *Example myofiber 1*). In stretching myofibers, some exhibited a pronounced increase in the distance between triads from the same sarcomere, with consecutive triads from adjacent sarcomeres maintaining their distance (Figure 10C, *Example myofiber 1*). In other cases, both triad distances increased in similar proportion (Figure 10C, *Example myofiber 2*). Arrows were graphed in Figure 10D (*Zoom in*) which highlight these variations detailed from example myofibers 1 (dotted arrows) and 2 (dashed arrows).

To better understand triad movement and its relationship with the SL variation during sarcomere contraction and stretching, we plotted values of DT-M and DT-Z against their corresponding SL across resting, contracting, and stretching states, covering a SL range of 1.68 to 4.16 µm (Figure 10D). The DT-M varied between 0.89 and 3.92 µm at the lowest and highest values of SL, respectively. The DT-Z variation occurred between 0.93 and 1.47 µm. Spearman's correlation analysis between DT-M and SL variation resulted in a statistically significant positive strong correlation ($\rho=0.85$, $p<0.0001$). For DT-Z no statistically significant correlation with SL variation was achieved ($\rho=0.32$, $p>0.20$).

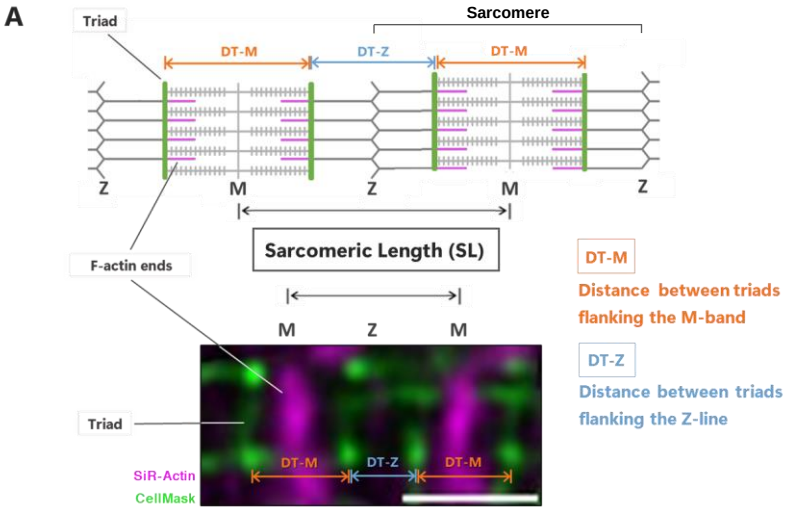
A
Triad
Sarcomere
DT-M
DT-Z
DT-M
Z
M
Z
M
Z
Sarcomeric Length (SL)
F-actin ends
DT-M
Distance between triads flanking the M-band
DT-Z
Distance between triads flanking the Z-line
M
Z
M
Triad
SiR-Actin
CellMask
DT-M
DT-Z
DT-M

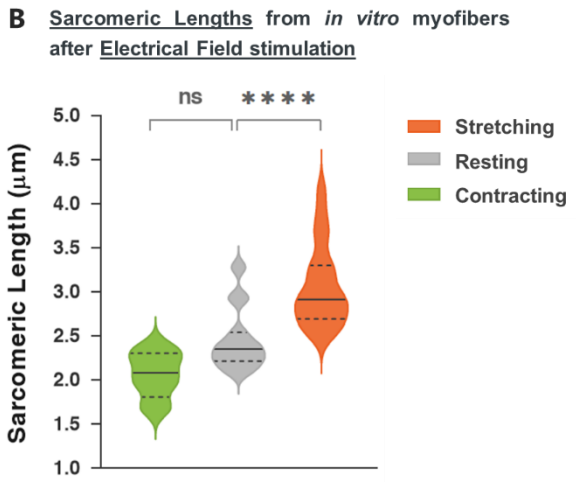
B
Sarcomeric Lengths from in vitro myofibers after Electrical Field stimulation
ns
****
Sarcomeric Length (µm)
5.0
4.5
4.0
3.5
3.0
2.5
2.0
1.5
1.0
Stretching
Resting
Contracting

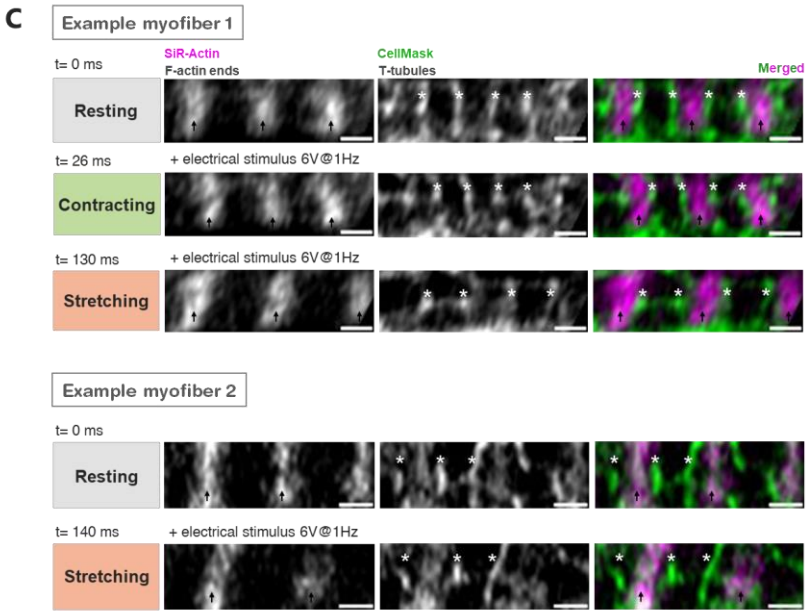
C
Example myofiber 1
t= 0 ms
SiR-Actin
F-actin ends
CellMask
T-tubules
Merged
Resting
t= 26 ms
+ electrical stimulus 6V@1Hz
Contracting
t= 130 ms
+ electrical stimulus 6V@1Hz
Stretching
Example myofiber 2
t= 0 ms
Resting
t= 140 ms
+ electrical stimulus 6V@1Hz
Stretching

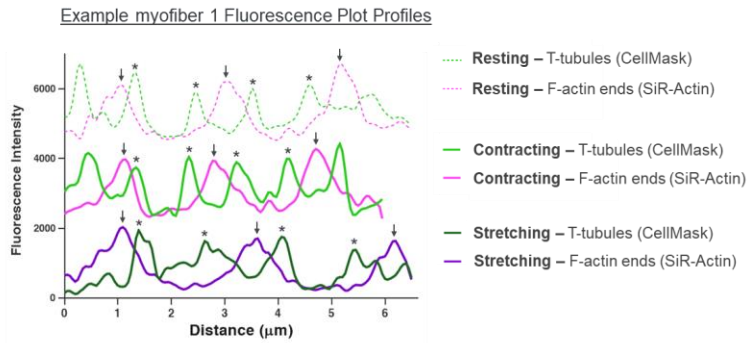
Example myofiber 1 Fluorescence Plot Profiles
Fluorescence Intensity
6000
4000
2000
0
0
1
2
3
4
5
6
Distance (µm)
Resting – T-tubules (CellMask)
Resting – F-actin ends (SiR-Actin)
Contracting – T-tubules (CellMask)
Contracting – F-actin ends (SiR-Actin)
Stretching – T-tubules (CellMask)
Stretching – F-actin ends (SiR-Actin)

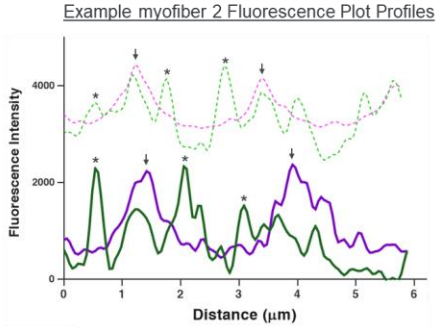
Example myofiber 2 Fluorescence Plot Profiles
Fluorescence Intensity
4000
2000
0
0
1
2
3
4
5
6
Distance (µm)

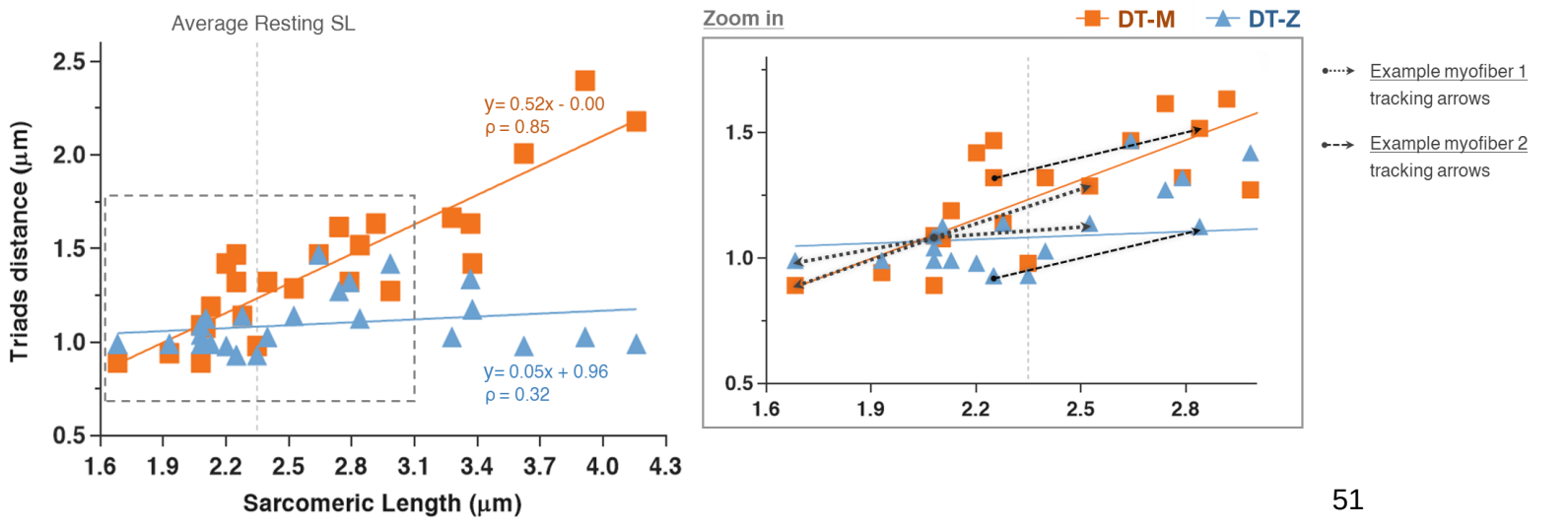
D
Triad distance over sarcomeric lengths achieved after in vitro Electrical Field stimulation
Average Resting SL
y= 0.52x - 0.00
ρ = 0.85
y= 0.05x + 0.96
ρ = 0.32
Triads distance (µm)
2.5
2.0
1.5
1.0
0.5
1.6
1.9
2.2
2.5
2.8
3.1
3.4
3.7
4.0
4.3
Sarcomeric Length (µm)
Zoom in
DT-M
DT-Z
1.5
1.0
0.5
1.6
1.9
2.2
2.5
2.8
Example myofiber 1 tracking arrows
Example myofiber 2 tracking arrows

Figure 10. Asymmetry in the dynamics of triad relative distance during sarcomeric length (SL) variation. **A.** Representative schematic image and microscopy image of SiR-Actin (magenta) and CellMask (green) labelled resting myofibers. Measurements taken are specified within both these images. **B.** Quantification of myofibers' SL (µm) during resting state or after electrical stimulus, which produced both lengthening and shortening of sarcomeres (n=6 sarcomeres of contracting myofibers, n=23 in resting, n=20 in stretching, N=10 myofibers). Statistical analysis with Wilcoxon matched pairs signed rank test, ******* p <0.001; n.s. p >0.0625. **C.** Representative images and respective fluorescence intensity plot profile from two distinct myofibers after electrical field stimulation. Example myofiber 1, undergoes contraction followed by stretching. Example myofiber 2 only stretches. T-tubules (asterisks) and F-actin ends (arrows) are labelled with CellMask (green) and SiR-Actin (magenta), respectively. **D.** Graphical plot of distances between triads of the same sarcomere, flanking the M-band (DT-M, orange squares) and from adjacent sarcomeres, flanking the Z-line (DT-Z, blue triangles). Graph includes all recorded measurements, independently of SL minimum or maximum values (n=14 sarcomeres). Graph on the right is a zoom-in that highlights singe-sarcomere variation of triad distance (DT) measurements in Example myofiber 1 (dotted arrows, origin in resting values and pointed ends towards contracting and stretching values) and in Example myofiber 2 (dashed arrows, origin at resting values and pointed end towards stretching values). All scale bars 1µm.

Furthermore, a linear regression analysis revealed a significant positive correlation between DT-M and SL, with a slope of 0.52 (r^2=0.80, p<0.0001). Once again, DT-Z did not demonstrate a statistically significant linear correlation with SL, as evidenced by a slope of 0.05 (r^2=0.05, p>0.20). The corresponding best-fit lines were represented along with the data in Figure 10D. Contrary to our initial hypothesis, DT-M revealed a strong linear correlation with SL variation, meaning that triads within the same sarcomere become closer and farther apart during contraction and stretching, respectively. On the other hand, DT-Z values remained relatively constant implying that triads from adjacent sarcomeres maintain their distance to each other during SLs changes.

It is worth mentioning that, despite imaging more than 20 myofibers from three distinct batches, the identification of transversal T-tubules (triads) in the patterned *in vitro* system proved challenging. Thus, we complemented our results with measurements from myofibers cultured in the unpatterned *in vitro* system already established by Pimentel, *et al* (2017) having a total of 14 myofibers analysed.

4.4. Whole muscle *ex vivo* induction of contraction and stretching corroborates asymmetrical variation of distance between triads.

To mitigate potential bias derived from the varying degrees of myofiber maturation observed within *in vitro* cultures, we used whole TA muscles from adult mice where different sarcomeric lengths were induced *ex vivo* (see *Material and Methods*). To induce contraction, freshly dissected muscles were incubated with potassium chloride (KCl) at 100 mM, 140 mM and 180 mM[62,86]. To induce stretching, muscles were first incubated with *d*-Tubocurarine (*d*-TC), an antagonist of ACh receptors which blocks muscle contraction. Subsequently, muscles were manually stretched until they increased their length by 1, 2 and 3 mm. However, for muscles stretched up to 3 mm, tendons detached from tibia bone, preventing further measurements. Afterwards muscles were fixed in PFA, freezed and longitudinally sectioned. Muscle cuts displayed many areas where the membrane network appeared well preserved, but others where disruption was visible, particularly towards the muscle's centre. Since this could be seen in all conditions, we believe it can be improved by increasing fixative concentration and prolonging incubation time. Next, cuts were stained with JPH1 and α-Actinin antibodies to measure triad distances and SL, respectively. Note that α-Actinin labels Z-lines, thus SL measurements in this case were done from Z-line to Z-line (in the *in vitro* results, SL is measured from M-band to M-band). In total, we quantified between 85-95 sarcomeres per each muscle state (control, contracted, stretched) from eight distinct mice. On average, SL from control muscles measured 2.00 µm (SL_0).

Contracted muscles displayed a similar reduction in muscle length across all KCl concentrations, averaging a 4mm decrease (Figure 11A). At the sarcomeric length level, a lower value was attained with KCl concentrations of 180 mM, with an average of 1.55 µm, compared to 100 mM or 140 mM, that reached 1.66 µm and 1.68 µm, respectively (Figure 11B). These values corresponded to a shortening of 23-16% in relation to the average SL in control conditions. Stretched muscles maintained their integrity (Figure 11A), yielding an average SL of 2.26 µm for a 1mm stretch and 2.54 µm for 2mm (Figure 11B). Thus, we reached an average stretching of 27-13%

compared to the SL in control conditions. For further data analysis, we focused on muscles contracted with 180 mM and 140 mM, stretched 2 mm and from control conditions. We excluded muscles contracted with 100 mM and stretched 1mm because their SL range is also obtained within samples from contracted 140 mM and stretched 2 mm, respectively.

Comparing the fluorescence intensity plot profiles of contracted muscles with control revealed that triads within the same sarcomere become closer together than consecutive triads from adjacent sarcomeres, which seemed to maintain their distance (Figure 11C, *Contracted muscle*). Conversely, stretched muscle plot profiles exhibited an increase in the distance between triads within the same sarcomere and a minor increase from triads between adjacent sarcomeres (Figure 11C, *Stretched muscle*).

Overall, after plotting all values of DT-M and DT-Z against the corresponding SLs obtained from each condition, a Spearman's correlation test indicated a strong positive correlation for DT-M (ρ=0.88, $p<0.0001$) and a moderate positive correlation for DT-Z (ρ=0.58, $p<0.0001$). Additionally, a subsequent linear regression analysis concluded that DT-M had a strong positive linear correlation with SL, bearing a slope of 0.67 (r^2=0.76, $p<0.0001$). And DT-Z also attained a positive linear correlation with SL, but the linear regression slope was 0.29 (r^2=0.39, $p<0.0001$). Best-fit lines were plotted with the data in Figure 11D.

Although DT-M displays an evident linear relationship with SL variation, DT-Z appears to maintain a more constant profile within a certain range, outside of which DT-Z values decrease or increase drastically, respectively. In mouse TA muscles, the physiological range of sarcomere motion, as referenced in the literature, was identified as being between 1.60 – 2.50 µm in SL (0.80 – 1.25 SL_0)[87,88]. By restricting DT analysis within this physiological SL range, we obtained a strong positive correlation for DT-M (ρ=0.82, $p<0.0001$), but a weak correlation for DT-Z (ρ=0.23, $p<0.01$). As for the linear regressions, DT-M produced a slope of 0.83 (r^2=0.67, $p<0.0001$) and DT-Z a slope of 0.14 (r^2=0.06, $p<0.01$). This second analysis emphasised a similar variation profile of DT to that

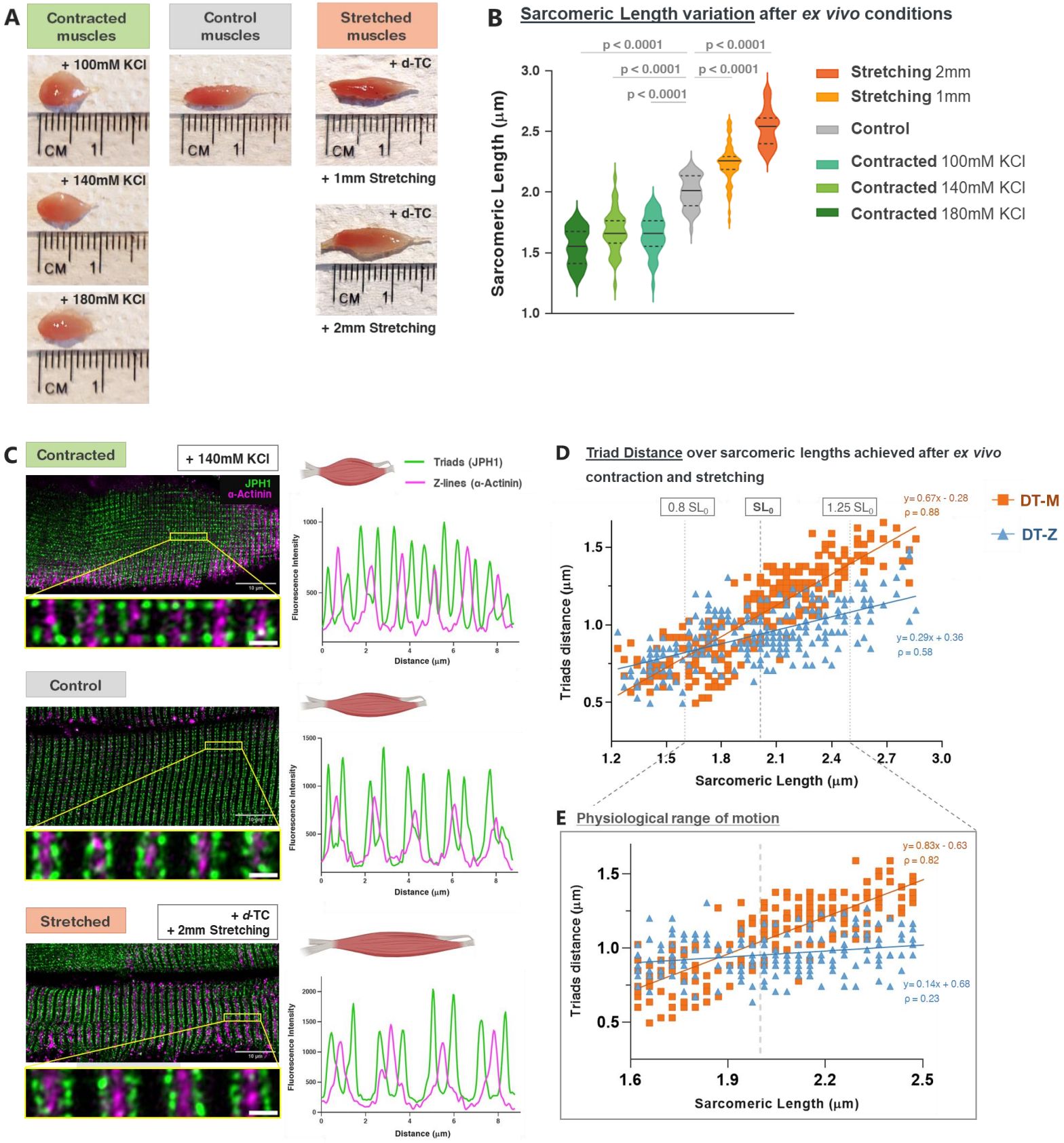
A
Contracted muscles
Control muscles
Stretched muscles
+ 100mM KCl
+ 140mM KCl
+ 180mM KCl
+ d-TC
+ 1mm Stretching
+ d-TC
+ 2mm Stretching
B
Sarcomeric Length variation after ex vivo conditions
p < 0.0001
p < 0.0001
p < 0.0001
p < 0.0001
p < 0.0001
Sarcomeric Length (µm)
Stretching 2mm
Stretching 1mm
Control
Contracted 100mM KCl
Contracted 140mM KCl
Contracted 180mM KCl
C
Contracted
+ 140mM KCl
JPH1
α-Actinin
Triads (JPH1)
Z-lines (α-Actinin)
Fluorescence Intensity
Distance (µm)
Control
Stretched
+ d-TC
+ 2mm Stretching
D
Triad Distance over sarcomeric lengths achieved after ex vivo contraction and stretching
0.8 SL0
SL0
1.25 SL0
y = 0.67x - 0.28
ρ = 0.88
y = 0.29x + 0.36
ρ = 0.58
DT-M
DT-Z
Triads distance (µm)
Sarcomeric Length (µm)
E
Physiological range of motion
y = 0.83x - 0.63
ρ = 0.82
y = 0.14x + 0.68
ρ = 0.23
Triads distance (µm)
Sarcomeric Length (µm)

Figure 11. Adult mouse whole-muscle experiments after ex vivo KCl-induced contraction or manual stretching, reveal a similar triad positioning profile to in vitro results, but only within the physiological range of motion for this muscle.

A. Adult mice TA muscles exposed to ex vivo conditions for contraction induction – 100mM, 140mM and 180mM KCl –, for stretching – d-Tubocurarine chloride (d-TC) + manual stretch of 1 and 2 mm –, and control conditions. **B.** Quantification of sarcomeric lengths (SL, µm) achieved with each ex vivo condition (n=279 sarcomeres, N=5 mice). Statistical analysis done with Mann-Whitney test. **C.** Representative immunostainings of fixed adult mouse whole-muscle after ex vivo KCl-induced contraction (140mM KCl), control and manual stretching with d-tubocurarine incubation (d-TC, 1µg/ml), from top to bottom. Antibodies used were anti-α-Actinin (Z-lines, magenta) and anti-JPH1 (Triads, green). Scale bars 1µm. For each condition, we plot on the right an intensity plot profile of each representative zoom in. **D.** Graphical plot of distances between triads of the same sarcomere, flanking the M-band (DT-M, orange squares) and from adjacent sarcomeres, flanking the Z-line (DT-Z, blue triangles) at a given sarcomeric length in a range between 1.23-2.86 µm. Myofibers quantified from four conditions: Stretch 2mm, Control, Contraction 140mM and 180mM KCl. On average, sarcomeric length from control muscles measured 2.00 µm (SL_0), which is highlighted at the graph. Moreover, minimum and maximum sarcomeric lengths that delineate the physiological range of mouse TA muscle (0.80 – 1.25 SL_0) are also highlighted. Linear regressions are plotted for both DT-M and DT-Z, and the Spearman's coefficients (ρ) are reference for each correlation (n=268 sarcomeres, N=8 mice). **E.** Zoom in of the previous graph within the physiological range of motion for TA muscle (see Results for more details). Linear regressions and Spearman's coefficients were re-done keeping only sarcomeric lengths between 1.60-2.50 µm (0.80 – 1.25 SL_0) and are plotted in the graph. Interestingly, within the physiological range, triads show a similar positioning profile in ex vivo compared to in vitro results – DT-M strongly correlated linearly with sarcomeric length, while DT-Z did not. Below this SL range, values from the distance between triads from adjacent sarcomeres (DT-Z) drastically decrease, and the opposite is true for values of sarcomeric length above the range. This suggests that triads do not remain tethered to the A-I junction during sarcomere movement, with their profile resembling the elastic dynamics of N2A element from Titin giant protein (see Results and Discussion for more details).

confirmed from live cell *in vitro* data. Herein, we showed that myofibers matured *in vivo* also reveal a linear variation in the distance between triads of the same sarcomere (DT-M) with SL changes, while triads from adjacent sarcomeres keep their distance relatively constant. Altogether, our data established that triads do not stay tethered at the A-I junction during sarcomere movement, which indicates that the potential link between triads and myofibrils is not specific to this sarcomeric region.

Outside the physiological range, DT-Z drastically decreases and increases at lower and higher SLs, respectively. This nonlinear profile of DT-Z is further dissected in the *Discussion* section.

5. Discussion

Skeletal muscle myofibers are highly organised cells composed of contractile sarcomeres. The correct positioning within the sarcomere of membrane structures associated with excitation-contraction coupling, such as triads, is essential for a synchronised muscle contraction. In mammalian skeletal myofibers, triads locate at the A-I junction where sarcomeric filaments overlap. This positioning of triads has been shown to promote faster excitation-contraction speeds when compared to other species where triads align with the Z-lines, as observed in frog skeletal myofiber[34]. But the question remains on triads positioning during myofiber synchronous contraction, where multiple sarcomeres reduce their sarcomeric length (SL) in synchronicity.

The correlation between SL variation and triad positioning has been previously explored in fixed skeletal myofibers after induced stretch or contraction. Studies on isolated rat myofibers revealed that triads remain close to the A-I junction despite increasing lengths, since the distance between Z-lines and triads (ZT or DT-Z) also increases[86]. These results support the hypothesis of a potential elastic tethering of triads to this sarcomeric region, although concerns about procedural artefacts have been raised due to the chemical skinning of used myofibers. On the other hand, in experiments with intact feline myofibers subjected to increasing SL, the DT-Z values remain constant. Thus, triads appear to move in conjunction with Z-lines, indicating a possible attachment to a more mobile sarcomeric component or solely to the SR itself[89]. *Ex vivo* imaging and manipulation of fixed myofibers has therefore produced conflicting results, highlighting the importance of live-cell imaging to study the dynamics of triad positioning during SL variation.

5.1. *In vitro* system suitable for live single-sarcomere imaging during skeletal myofiber contraction.

Within this project we established an *in vitro* system capable of generating mature skeletal myofibers and promote their unidirectional alignment and individualisation. As described in *Material and Methods,* we combined a protocol of primary mouse

myoblast isolation and differentiation, with a UV micropatterned linear substrate to grow myofibers within parallel linear regions. Overall, our cultures in the patterned system exhibited the intended alignment and individualised myofibers could be obtained. Additionally, the number of mature myofibers expressing transversely aligned JPH1 (SR-associated triadic protein) was similar between patterned and unpatterned *in vitro* systems. During experimental imaging, we struggled to find mature myofibers expressing organised T-tubules, particularly within the patterned system. This contradicts the results obtained from the initial analysis of mature myofibers in patterned and unpatterned systems, where JPH1was used as a reporter for transversal triads. However, during mammalian triad biogenesis SR-associated triadic proteins organise at the A-I junction during embryonic development, while the transversal alignment of T-tubules in this region only occurs postnatally. This could explain why our initial assessment of myofiber maturity through JPH1 localisation did not seem representative of the observed number of myofibers showing proper alignment of T-tubules during live-cell imaging, especially at the patterned system.

Optimisations were performed to improve myofiber adhesion to the patterns. For example, coating adhesion regions with 10% or 1% Matrigel, or with Matrigel and Fibronectin, although the number of mature adhered myofibers at imaging days did not improve (data not shown). We also tested different topcoats of 50% to 100% Matrigel and 1% to 1.5% agarose. Agarose topcoats did not properly adhere to the patterned coverslips, but higher concentration Matrigel showed a slight improvement in the number of adhered myofibers, with no visible effects on contraction.

Therefore, coupling this patterned *in vitro* system with super-resolution microscopy and the appropriate molecular tools for live-cell imaging, demonstrates great potential for studying myofiber dynamic events, such as myofiber development, nuclear movement or cell migration. Unfortunately, for studies that require long-term cell culture or complete myofiber maturation, as is the case with studies requiring matured triads, our patterned *in vitro* system may not be optimally effective. To address this issue of imaging triad positioning in live primary myofibers, we could switch to *in vivo* matured myofibers isolated from adult mice. After inducing

contraction through electrical field stimulation, triads would be tracked relative to SL using the same live-cell imaging setup.

5.2. High-speed imaging of contracting myofibers reveals both shortening and stretching of individual sarcomeres.

We recorded time-resolved myofiber contractions with super-resolution fluorescence microscopy using the Zeiss Multiplex SR-4Y mode. When acquiring a single channel, we achieved a frame rate of 100 Hz, enabling a comprehensive assessment of the complete range of SL variations during both spontaneous and electrically induced contractions. From the few spontaneous contractions observed, sarcomeres seem to shorten and rapidly return to resting state (Figure 9B), while in electrically induced contractions both sarcomere shortening and stretching was revealed (Figure 9D). Some sarcomeres exclusively undergo stretching, others shortening preceded or followed by stretching. Our electrical stimulation protocol consisted of single twitch pulses with 1Hz frequency and 6V. This condition increased the temporal resolution of sarcomere movement imaging during contraction events, especially when compared to optogenetic stimulation (Figure 9C). Moreover, it did not induce myofiber fatigue as previously expected.

Interestingly, observations of *in vitro* tetanic stimulation of fixed-end single frog skeletal myofibers have shown that a sarcomeric tendency for lengthening after stimulation correlated with higher resting SL values, above 2.55 µm[90]. Within our patterned *in vitro* system, overall higher resting SLs were discerned, with all sarcomeres stretching and only 2 out of 5 also undergoing shortening, in particular those with resting SL values below 2.55 µm. As outlined in the *Results* section, myofibers from unpatterned *in vitro* system were also integrated into these results. Notably, these myofibers exhibited on average lower resting SLs (< 2.55µm), yet all analysed sarcomeres underwent stretching, with only 3 out of 17 shortening prior to lengthening. Considering these outcomes, we believe that our patterned *in vitro* system may elicit a more physiologically relevant contraction in skeletal mouse myofibers than the unpatterned system, post electrical stimulus.

Studies focusing on single-sarcomere dynamics in both cardiac and skeletal myofibers demonstrated that during induced isometric contractions, sarcomeres exhibit a non-uniform SL variation. Kobirumaki-Shimozawa, *et al.* (2021) demonstrated this phenomenon in *in vivo* mouse heart, highlighting the cyclical nature of sarcomeres as they undergo sequential shortening and stretching due to the tug-of-war mechanism activated in response to a rise in Ca^{2+}[91]. Telley, *et al* (2006) used fixed-end rabbit isolated skeletal myofibrils to induce single-sarcomere contractions by locally elevating Ca^{2+}. Their observations indicated significant variability in shortening velocities and resting SLs of individual sarcomeres along myofibers, which were identified as major contributors to the non-uniform behaviour of stimulated sarcomeres[31,92]. The intrinsic variability in individual sarcomere responses might have hindered our ability to capture synchronous contractions within our experimental setup. To the best of our knowledge, this heterogeneous SL variation during electrically induced contractions is being documented for the first time in an *in vitro* primary mouse skeletal myofibers system.

For further analysis of triad positioning during contraction and stretching of sarcomeres, we employed dual-channel microscopy imaging both F-actin and T-tubules. This allowed a direct comparison of distance variation between the triads of the same sarcomere and those of adjacent ones. Despite a decreased frame rate of 71-77 Hz, this microscopy approach provided sufficient time resolution to measure SLs and DTs at peak time-points of shortening, lengthening, and resting.

Nevertheless, in our future work we aim to enhance the number of contracting myofibers and extend the duration of contraction by refining the electrical stimulation protocol. We plan to transition from twitch pulses to tetanic stimulation through an increase of pulse frequency to achieve between 25-50Hz[93,94]. Prolonging the contraction period in myofibers could also improve both spatial and temporal resolution. Extending this contracted state amplifies the timeframe available for capturing high-resolution images, thus augmenting the quantity of photons emitted from fluorescent labels, which also improves signal to noise ratio.

5.3. Asymmetrical distance variation among triads challenges initial hypothesis of triad tethering at the A-I junction.

To gain insights into the dynamic nature of triad positioning at the A-I junction, we induced sarcomere shortening/stretching and correlated it with the observed distances between triads. To precisely locate triads within the sarcomere during these dynamic events, we distinguished two measurements of triads distance: distance between triads within the same sarcomere, where they flanked the M-band (DT-M); and between triads from adjacent sarcomeres, which flanked the Z-lines (DT-Z). These measurements can be compared to others referenced in existing literature, such as distance between triads and M-band (MT) and between triads and Z-line (ZT), respectively[89].

Our findings, derived from time-resolved super-resolution live tracking of triads, highlight a stronger correlation between SL variation and the DT-M compared to the DT-Z, where no statistically significant correlation could be inferred. In other words, during contraction/stretching, the distance between triads from adjacent sarcomeres, that flank Z lines, remains fairly constant. On the other hand, the distance between triads of the same sarcomere, that flank the M-band, decreases and increases in a positive linear manner with SL variation (DT-M varies by half a micron for every 1 µm increment of SL). From the Pearson's correlation we can suggest that 80% of DT-M variation can be attributed to SL variation (Figure 10D).

For triads to remain positioned at the A-I junction, our experimental results should have shown DT-M remaining constant with SL variation and a linear regression slope of about 0.5 for the DT-Z. Instead, the complete opposite was detected, with DT-Z showing little variation within a physiological range of SLs and DT-M varying linearly with SL changes (*in vitro* data revealed a slope of 0.52 for DT-M; *ex vivo* a slope of 0.84). From this general analysis, we can infer that triads within the same sarcomere move towards the M-band during sarcomere shortening, and away from this region during stretching. Moreover, the distance between triads from adjacent sarcomeres remains relatively constant, which might be due to the concurrent variation of I-band width during SL changes (explained in section 1.1.1). Essentially, triads do not stay

positioned at the A-I junction during sarcomere shortening and lengthening (Figure 12).

Mature myofibers within our *in vitro* system exhibit varying degrees of membrane network organisation, even though all quantified myofibers displayed transversally aligned T-tubules. Therefore, we also assessed triad positioning during contraction/stretching using *in vivo* matured myofibers, which display complete triad organisation. We performed super-resolution fluorescence imaging of adult mouse TA muscles after *ex vivo* chemical induction of contraction and manual stretching.

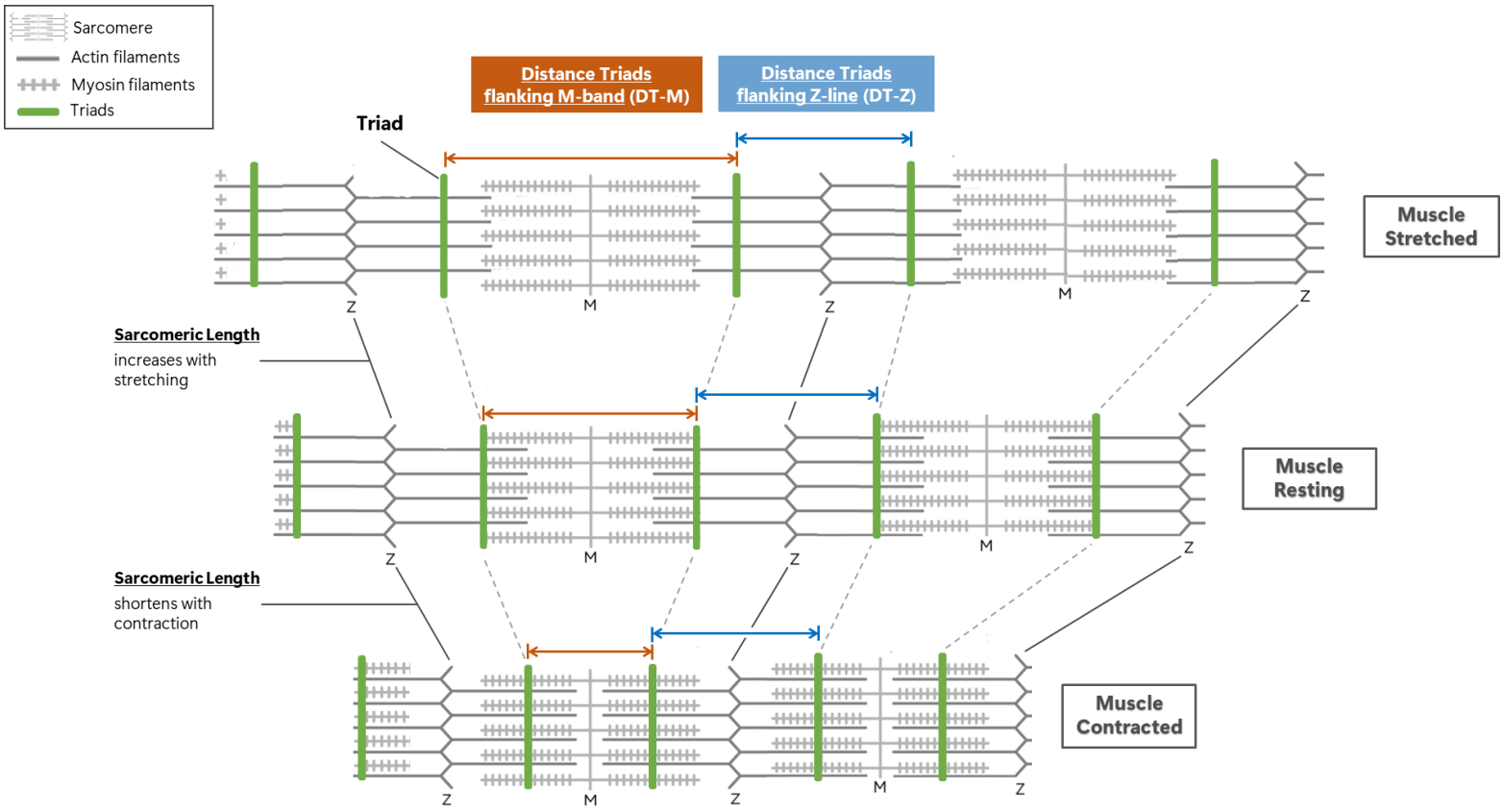

Figure 12. Conceptual model illustrating triad positioning dynamics in skeletal muscle during stretching and contraction.

In mammalian skeletal muscle, triads localise at the A-I junction, the interface of actin and myosin filaments overlapping region. During muscle contraction and stretching the actin filaments slide through the myosin (cross-bridge cycle) towards the centre of the sarcomere or away from it, respectively. This culminates in the shortening of sarcomeres (decreased Sarcomeric Length (SL)) or lengthening (increased SL), respectively. From our results obtained with in vitro primary skeletal myofibers and ex vivo whole-muscles, we confirmed that triads do not remain tethered at the A-I junction during sarcomere shortening and stretching. By measuring and comparing the distance between triads from the same sarcomere, flanking the M-band (DT-M), and triads from adjacent sarcomeres, flanking the Z-line (DT-Z), we inferred that triads exhibited a dynamic positioning, invading the myosin filament region during shortening and distancing from it during stretching.

Data gathered from all *ex vivo* experiments spanned a range of 1.23 to 2.86 µm in SL. The use of increasing concentrations of potassium chloride (KCl) to induce contraction allowed us to achieve lower SLs than those seen *in vitro* with electrical twitch stimulation (minimum *in vitro* SL was 1.60 µm). Notably, these values extend beyond the physiological limits of sarcomere shortening for TA muscle[87](Figure 11D).

Once again, we observed strong correlation between DT-M and SL, with plotted linear regression showing a slight increased slope compared to *in vitro* results. Regarding DT-Z, a moderate positive correlation with SL was obtained which did not corroborate our *in vitro* live cell observations. However, we repeated this correlation analysis now restricting SL values to the physiological range of motion for mouse TA muscles referenced in the literature, between 1.60 – 2.50 µm (0.80 – 1.25 SL_0) [87,88]. The DT-M maintained its strong correlation with SL, but this time the DT-Z exhibited a weak correlation and a linear regression slope more similar to that of *in vitro* analysis. These results give some indication that triads change their positioning properties in SLs beyond the 0.80 – 1.25 SL_0 physiological range. Notably, we still observed great variability of our DT-Z data within the SL physiological range, which may mask some more detailed triad distance variation (Figure 11E).

From the live *in vitro* tracking of triad positioning, we expanded our analysis into the triad distance of single sarcomeres during time-resolved shortening and stretching. Single-sarcomere tracking revealed a reduction of DT-Z in shortening sarcomeres, although to a lesser extent than the decrease observed in DT-M (Figure 10D, *Zoom in*, *Example myofiber 1*). This repositioning of triads during sarcomere shortening is not evidently expressed in our fit regressions and correlations. Unfortunately, we only captured shortening sarcomeres from one myofiber and therefore these results may not be representative of the whole population. Our *ex vivo* experimental work showed little variation in DT-Z of contracted muscles compared to control for physiological SLs (SL> 1.60 µm), but below this SL value we attained a decrease of DT-Z in both muscles incubated with 140 mM and 180 mM KCl, ruling out the possibility of procedural artefacts. The observation of a reduction in DT-Z below this

SL value suggests that a potential mechanism maintaining equidistant triads of adjacent sarcomeres during shortening may be disrupted at non-physiological SLs.

Single-sarcomere tracking of live stretching myofibers highlighted some sarcomeres showing no variation in DT-Z (Figure 10D, *Zoom in*, *Example myofiber 1*), while others exhibited an increase of this value similar to that observed in their paired DT-M (Figure 10D, *Zoom in*, *Example myofiber 2*). Cross-referencing these observations with our *ex vivo* data, a slight increase in DT-Z could be discerned with increasing SLs. Notably, within the physiological SL range, we still detected great variance in DT-Z, with some values surpassing those of DT-M from the same SL. This variance resembles the movement profiles observed through single-sarcomere analysis *in vitro*, where some triads distance more from the Z-lines and others maintain this same distance more constant. We remain uncertain of the possible biological meaning of this disparity between DT-Z values.

Altogether, our findings provide evidence of triad repositioning away from the A-I junction, displacing towards the M-band during sarcomere shortening. During stretching, triads move away, maintaining relatively constant their distance to the Z-lines, at least in physiological ranges of sarcomere motion (Fig. 12). Our results are in line with other published work that correlates triad positioning with SL variation using electron microscopy (EM)[35,89]. In Brown, *et al* (1998) experiments with feline skeletal muscle revealed that MT varies proportionately with SL variation, while ZT remains relatively constant throughout their SL range. EM images also show triads moving from the A-I junction into A or I-bands at reduced and increased SLs, respectively. Interestingly, their ZT values display an increase around the SL of 1.80 µm which is also noticeable in our DT-Z distribution. We are unsure if it holds any biological significance, although in both studies this coincides with the abrupt decrease in MT/ DT-M to values below those measured for ZT/DT-Z. This pattern suggests a potential natural “pulling” of triads away from Z-lines due to this lower DT-M reached.

Given the present body of work, we believe that triads are tethered to the myofibrils through an A-I junction independent anchor. To better understand the properties of

this interaction, we intend to improve our *in vitro* live-cell imaging design by switching our model to isolated mouse skeletal myofibers. It will grant the possibility of studying triad positioning in a single myofiber presenting an *in vivo* developed membrane network and with a contractile response to electrical stimulus. Moreover, implementing a tetanic stimulation protocol could prolong sarcomere shortening and, ideally, reach a lower range of SLs (non-physiological). This could also improve imaging time-resolution during sarcomere shortening compared to what we attained presently by inducing twitch contractions.

This isolated myofiber *in vitro* system may be useful in the pursuit of future questions on potential tethering partners of triads. Knocking down possible triad interactors, using electroporation and siRNA, and reassessing the dynamics of triad positioning would give us insight on the molecular interactors responsible for the contact between triads and myofibrils. All the technical expertise achieved during this project and available at the lab would grant us the necessary tools to perform these future experiments.

5.4. Potential triad interactors bridging the gap with myofibrils.

Based on current literature, we can speculate on potential triad interactors that may be linking them to the myofibrils. As previously discussed, triads undergo repositioning during sarcomeric length variation, seemingly in tandem with the movement of Z-lines. Therefore, the anchoring of triads to the myofibrils likely involves sarcomeric proteins that retain their distance from the Z-line and, consequently, exhibit higher variation in their distance to the M-band throughout sarcomeric length changes.

We propose the tethering of triads to the giant protein Titin, particularly at the N2A region. Titin spans from Z-line to M-band in each half-sarcomere, serving as a scaffold that establishes a “molecular blueprint” for the coordinated integration of sarcomeric components into the intricate structure of sarcomeres. Moreover, Titin confers elastic properties to the sarcomere, with the I-band region of Titin acting as molecular spring that, when extended, develops passive force. Conversely, A-band

region is highly repetitive and relatively inextensible (reviewed in Gregorio, *et al* (1999))[7]. Interactions between Titin and the SR membranes have been documented at the M-band, facilitated by obscurin-ank1.5 interaction [11,95,96]. This opens a precedent for a possible molecular link between Titin and the membranes that comprise the triads.

We reviewed Titin's elastic regions at the I-band and binding proteins known to interact with either SR or T-tubule membrane. Four springlike elements from this I-band region have been described: tandem Ig-domains, the PEVK motifs, the N2A element (present in all striated muscles) and the N2B element (exclusive of cardiac muscle)[5]. Studies aiming to better understand each element's elastic properties have revealed different extension ratios between them during skeletal muscle stretching[97–99]. By comparing the distance between each element and the Z-line to our values of DT-Z, we assessed that the N2A element displays an extension profile similar to that observed in our *ex vivo* data. From two independent studies in rabbit skeletal muscle, the distance from N2A to Z-line has been calculated to increase in ~ 0.25 μm between SLs of 2.00–2.50 μm and is followed by a plateau that persists until 3.00 μm in SL. Between 2.50 and 3.00 μm, occurs the extension of the PEVK region, which has shown to be more extensible than the other Titin domains (Figure 13)[97]. From our *ex vivo* experiments, we obtained a similar correlation between SL variation and DT-Z, where a decrease at lower SLs (1.2-1.6 μm) is observed but at physiological SLs this distance presents a more constant profile, with a variation of ~0.14 μm. Additionally, measurements in rabbit skeletal muscle of the distance between the N2A element and the M-band at varied SLs (from 1.8 to 3.7 μm) obtained a linear correlation with a slope of 0.75[118]. Once again, from our *ex vivo* results a similar linear correlation between DT-M and SL variation is observed (~0.83 μm at physiological SL range).Hence, we believe that triads could be tethered either at the N2A element or at a region proximal to PEVK motifs, since extension of the latter would lead to a significant increase of DT-Z after SLs of 2.50 μm, not evident in our data. To pursue this hypothesis, we intend to first confirm triad co-localisation with one of these Titin domains through co-immunostainings. Then, assess and

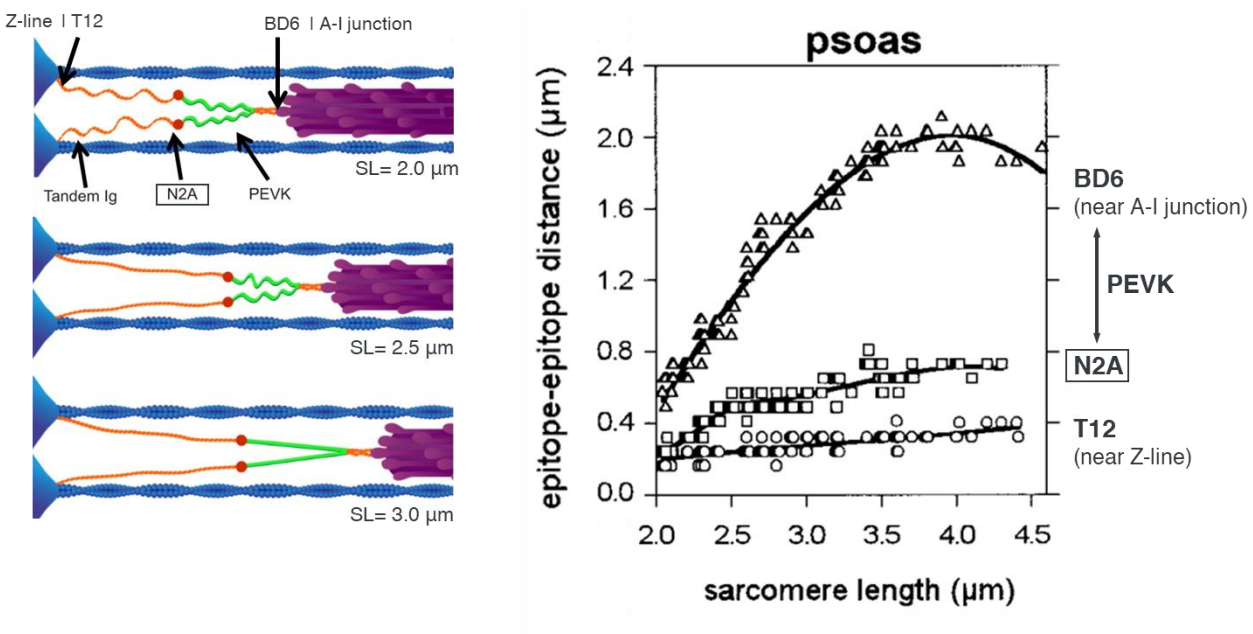

Figure 13. Titin I-band domains extension profiles relative to sarcomeric length (SL) variation.
Illustration of Titin domains – tandem Ig domains, N2A and PEVK – extension profile at SLs of 2.0 µm, 2.5 µm and 3.0 µm. It becomes clear that N2A distance from the Z-line increases slightly from 2.0 µm to 2.5 µm, but the PEVK domain presents a higher extension capacity right after N2A reaches its plateau (2.5 µm to 3.0 µm). From rabbit skeletal muscle, extension of each Titin domain was calculated during SL variation (in relation to the Z-line) and was plotted, revealing different extension ratios between domains. The T12 antibody binds a region of Titin near the Z-line and little extension is observed throughout the SL range; N2A domain slightly increases until the 2.5 µm and maintains a plateau at higher SLs; BD6 antibody stains a region near the A-I junction and its increased extension is mainly due to PEVK extension, which preceeds this domain. Both T12 and BD6 antibodies localisation relative to the sarcomere is illustrated on the schematic (left). Adapted from Nishikawa (2016) and Linke, et al (1996).

compare triad positioning dynamics in domain specific-Titin mutants. Additionally, reaching higher values of SL in *ex vivo* stretched muscles could help to further profile triad positioning variation and draw a better correspondence with the available profiles of Titin domains.

Recently, Lu, *et al* (2022) unveiled a novel function of the CMYA5 protein (or myospryn) as a key organiser of dyad architecture and positioning in cardiac muscle at the Z-line[100]. Their study confirmed the interaction and co-localisation between CMYA5 and dyadic proteins in mouse heart, particularly RYR2. They propose that CMYA5 first binds to the Z-lines and later tethers the RYR2-containing j-SR domains to this region through CMYA5–RYR2 interaction, followed by the subsequent annexation of T-tubules. In homozygous *Cmya5* knockout mice, they observed the disruption of transversal alignment of both j-SR and T-tubule marker proteins,

especially with FSD2 which is thought to be an interacting partner of CMYA5. Unsynchronised dyadic EC-coupling was also detected. Attempts to rescue CMYA5-KO hearts by expressing either FSD2 or CMYA5 protein fragment (that binds to RYR2) failed, likely due a necessary binding of CMYA5 to the Z-lines for its organiser function.

Could CMYA5 perform a similar role in mouse skeletal muscle? CMYA5 belongs to the A-kinase anchoring proteins (AKAPs) family and interacts with dystrophin at the costameres (Z-lines) connecting SR membrane and myofibrils[101]. Besides this positioning, in skeletal muscle CMYA5 has also been detected localising in doublets adjacent to Z-lines, which together with data observed in cardiac myofibers hints at a co-localisation with triads[102]. Furthermore, in dystrophin-deficient *mdx* mice, a model of human Duchenne muscular dystrophy (DMD) characterised by triad mislocalization, CMYA5 transcription levels are reduced compared with WT mice[103]. Human DMD-patient samples exhibit this same reduction of CMYA5 transcription, highlighting the potential role of CMYA5 in triad function and positioning in skeletal muscle[104]. Still, no microscopy data has been shown to confirm triad and CMYA5 co-localisation in skeletal muscle, and future work on this hypothesis should start here.

Nonetheless, newly discovered associations between CMYA5 and other triadic interactors can shed light into this putative co-localisation with triads. CMYA5 has been found to interact with calpain-3 (CAPN3/p94), a non-lysosomal cysteine protease that binds to RyR1 in mouse skeletal muscle[105]. Mutations in CAPN3 are the most frequent causes of limb girdle muscular dystrophy type 2A (LGMD2A), a myopathy characterised by muscle contraction dysfunction and sarcolemma disruption (reviewed in Gallardo, *et al* (2011))[106]. In CAPN3-KO mice the number of RYR1 is decreased and defects are seen in EC-coupling, but triad positioning is not disrupted[105]. Further studies confirmed that the proteolytic domain of CAPN3 is not the main responsible of these phenotypes, suggesting that it plays a role as a structural element of myofibrils and j-SR membranes[107]. This indicates that CAPN3 is not necessary for the potential triad positioning role of CMYA5, but they might

share a preferential binding site close to triad location. Interestingly, CAPN3 is preferentially expressed in skeletal muscle and almost absent in cardiac muscle, where triads position at the Z-lines[108]. This expression profile suggests a unique correlation between CAPN3 and the triad positioning at the A-I junction in skeletal muscle.

Furthermore, CAPN3 is known to bind to Titin's N2A element, between the I80-IS and the I81-I83 subdomains, and within the N2A-PEVK junction[109]. These regions are in close proximity to the A-I junction, where triads are positioned. This spatial overlap can be especially apparent with shorter sarcomeres due the folding properties of Titin. Once again, assessing co-localisation of N2A and PEVK elements with triads in skeletal muscle during contraction would be our next step.

Another potential candidate involved in triad anchoring is the striated preferentially expressed protein kinase (Speg). Mutations in this protein have been associate to concurrent CNM and cardiomyopathies in patients, where triads/dyads present defective positioning and function[110,111]. Mice skeletal myofibers with reduced levels of the Spegβ isoform showed an increase in the number of longitudinal triads, an indication of disruption in the link between triads and myofibrils[111]. From mice Speg-KO models a significant decrease was detected in RYR1, JPH1, CMYA5, Fsd2 (part of the CMYA5 complex) and Esd. All these proteins where also confirmed to directly bind to Spegβ[111]. Interestingly, Speg protein knockdown does not seem to affect DHPRα1 and SERCA1 protein levels, but in discrete areas of Speg-KO myofibers, these proteins were mispositioned[112].

Speg seems to play a role in localising these proteins to the triadic membranes, potentially acting upstream of the CMYA5 complex. But could Speg be the tethering link between triads and the myofibrils? Notably, this protein shares high structural homology with obscurin, a sarcomeric protein known to be involved in the link between myofibrils and the SR, at the costameres[11,113]. Similarly to obscurin, Speg is composed by the same arrangement of Kinase–like, Ig and Fibronectin(FN)-III domains, but displaying a longer "interkinase region" sequence[114]. Qadota, *et al* (2020) discovered that this "interkinase region" in *C. elegans* obscurin homologue,

UNC-89, exhibits spring-like properties and in-frame deletion mutation causes sarcomeric disorganisation with visible shorter A-band[115]. This same phenomenon can be seen with the deletion of Titin's super repeats[8,9].

In skeletal muscle, Speg interacts with the rod domain of desmin, an intermediate filament located at the Z-lines[112,116]. Collectively, we can hypothesise that Speg might act as a scaffold protein that tethers triads to the sarcomere via desmin interactions, potentially demonstrating similar elastic properties as the N2A domain in Titin. Further single molecule analysis of Speg elasticity should be conducted and compared to the dynamic profile of triad positioning concluded from this project.

6. Conclusions

Our findings contribute to the ongoing exploration into the dynamic interplay between myofibrils and the surrounding membrane network, particularly, the positioning of triads during skeletal muscle contraction and stretching events. By integrating high-speed super-resolution live-cell imaging into our *in vitro* skeletal myofibers system, we have successfully developed a platform for fast tracking of organelles and proteins during dynamic events. However, studying triad positioning *in vitro* posed challenges, such as the limited number of myofibers exhibiting organised T-tubules and lack of sarcomere shortening during electrical field stimulation.

Nevertheless, our *ex vivo* experiments with intact mouse skeletal muscle provided crucial insights into triad positioning within different sarcomeric lengths obtained from KCl-induced muscle contraction and manual stretching. Contrary to the initial hypothesis of triad tethering at the A-I junction, our results unveiled a dynamic localisation of triads, invading the thick filament region (A-band) during shortening and distancing from the M-band towards the I-band during stretching. Notably, the triad distance to the Z-lines stayed relatively constant within a physiological sarcomeric length range (1.60–2.50 µm). However, the distance between triads and Z-lines decreased at lower sarcomeric lengths and slightly increased at higher ones, mirroring the elastic behaviour seen with N2A element of Titin. This dynamic profile of triad positioning hints at a potential anchoring at the N2A element or N2A-PEVK junction mediated presumably by RYR1–CMYA5–CAPN3 interactions. We also discuss possible triad tethering to the Z-lines through Speg–CMYA5–Desmin binding, as Speg's protein structure exhibits elements with elastic properties similar to those of N2A.

The observed asymmetry in distance variation between triads/Z-lines and triads/M-band may provide insights into the less explored domain of sarcoplasmic reticulum (SR) behaviour during sarcomeric length variation. Structurally, the SR exhibits a longitudinal region (l-SR) that spans the entire length of myofibrils, differentiating into a transversal tubular shape at the A-I junction (junctional SR) where it interacts with the T-tubules to form triads. The characteristics of the l-SR enveloping a single

sarcomere (over the M-band region) compared to the l-SR around adjacent sarcomeres (over the Z-line) remain largely unexplored and this regional division of the l-SR is not typically considered by peers. Our data suggests that the l-SR over the Z-line does not change length while the l-SR over the M-band shortens or stretches during sarcomeric motion. This could indicate that these two l-SR regions exhibit distinct physical properties: the l-SR over the Z-lines may be less flexible, while the l-SR over the M-band region may present more elastic properties, which would allow it to stretch and shrink simultaneously with triads during sarcomere lengthening and shortening, respectively. Electron microscopy has revealed varying structural architectures of the SR, potentially correlating with these differential SR properties[24].

Our discoveries provide a basis for future investigations into the nature of the connection between triads and a putative sarcomeric protein. This is especially significant in the context of centronuclear myopathies, where triad disorganisation stands as a hallmark.

6. Bibliography

1. Marieb, E. N. & Hoehn, K. N. *Human Anatomy & Physiology*. (2007).

2. Squire, J. Special Issue: The Actin-Myosin Interaction in Muscle: Background and Overview. *Int. J. Mol. Sci.* 20, 5715 (2019).

3. Wang K, Wright J. Architecture of the sarcomere matrix of skeletal muscle: immunoelectron microscopic evidence that suggests a set of parallel inextensible nebulin filaments anchored at the Z line. *J. Cell Biol.* 107, 2199–2212 (1988).

4. Ohtsuki, I. & Morimoto, S. Troponin: Regulatory function and disorders. *Biochem. Biophys. Res. Commun.* 369, 62–73 (2008).

5. Kontrogianni-Konstantopoulos, A. *et al.* Muscle Giants: Molecular Scaffolds in Sarcomerogenesis. *Physiol. Rev.* 89, 1217–1267 (2009).

6. Freiburg, A. *et al.* Series of exon-skipping events in the elastic spring region of titin as the structural basis for myofibrillar elastic diversity. *Circ. Res.* 86, 1114–1121 (2000).

7. Gregorio, C. C. *et al*. Muscle assembly: a titanic achievement? *Curr. Opin. Cell Biol.* 11, 18–25 (1999).

8. Tonino, P. *et al.* The giant protein titin regulates the length of the striated muscle thick filament. *Nat. Commun.* 8, 1041 (2017).

9. Methawasin, M. *et al.* Shortening the thick filament by partial deletion of titin's C-zone alters cardiac function by reducing the operating sarcomere length range. *J. Mol. Cell. Cardiol.* 165, 103–114 (2022).

10. O'Neill, A. *et al.* Sarcolemmal Organization in Skeletal Muscle Lacking Desmin: Evidence for Cytokeratins Associated with the Membrane Skeleton at Costameres. *Mol. Biol. Cell* 13, 2347–2359 (2002).

11. Lange, S. *et al.* Obscurin determines the architecture of the longitudinal sarcoplasmic reticulum. *J. Cell Sci.* 122, 2640–2650 (2009).

12. Flucher, B. E. & Franzini-Armstrong, C. Formation of junctions involved in excitation-contraction coupling in skeletal and cardiac muscle. *Proc. Natl. Acad. Sci.* 93, 8101–8106 (1996).

13. Takekura, H. *et al*. Differentiation of membrane systems during development of slow and fast skeletal muscle fibres in chicken. *J. Muscle Res. Cell Motil.* 14, 633–645 (1993).

14. Reger, J. F. The fine structure of neuromuscular junctions and the sarcoplasmic reticulum of extrinsic eye muscles of Fundulus heteroclitus. *J. Biophys. Biochem. Cytol.* 10(4)Suppl, 111–121 (1961).

15. Golini, L. *et al.* Junctophilin 1 and 2 Proteins Interact with the L-type Ca2+ Channel Dihydropyridine Receptors (DHPRs) in Skeletal Muscle. *J. Biol. Chem.* 286, 43717–43725 (2011).

16. Phimister, A. J. *et al.* Conformation-dependent Stability of Junctophilin 1 (JP1) and Ryanodine Receptor Type 1 (RyR1) Channel Complex Is Mediated by Their Hyper-reactive Thiols *. *J. Biol. Chem.* 282, 8667–8677 (2007).

17. Ito, K. *et al.* Deficiency of triad junction and contraction in mutant skeletal muscle lacking junctophilin type 1. *J. Cell Biol.* 154, 1059–1068 (2001).

18. Hirata, Y. *et al.* Uncoupling Store-Operated Ca2+ Entry and Altered Ca2+ Release from Sarcoplasmic Reticulum through Silencing of Junctophilin Genes. *Biophys. J.* 90, 4418–4427 (2006).

19. Fujise, K. *et al*. Centronuclear Myopathy Caused by Defective Membrane Remodelling of Dynamin 2 and BIN1 Variants. *Int. J. Mol. Sci.* 23, 6274 (2022).

20. Al-Qusairi, L. & Laporte, J. T-tubule biogenesis and triad formation in skeletal muscle and implication in human diseases. *Skelet. Muscle* 1, 26 (2011).

21. Al-Qusairi, L. *et al.* T-tubule disorganization and defective excitation-contraction coupling in muscle fibers lacking myotubularin lipid phosphatase. *Proc. Natl. Acad. Sci.* 106, 18763–18768 (2009).

22. Smith, C. *et al*. Physiology and patho-physiology of the cardiac transverse tubular system. *Curr. Opin. Physiol.* 1, 153–160 (2018).

23. Quinn, C. J. & Dibb, K. M. The origin of T-tubules. *eLife* 12, e88954 (2023).

24. Hayashi, K. *et al*. Three-dimensional architecture of sarcoplasmic reticulum and T-system in human skeletal muscle. *Anat. Rec.* 218, 275–283 (1987).

25. Paolini, C. *et al*. Evidence for conformational coupling between two calcium channels. *Proc. Natl. Acad. Sci.* 101, 12748–12752 (2004).

26. Franzini-Armstrong, C. Functional implications of RyR-DHPR relationships in skeletal and cardiac muscles. *Biol. Res.* 37, 507–512 (2004).

27. Clarke, M. Muscle sliding filaments. *Nat Rev Mol Cell Biol 9 Suppl 1 S7* (2010).

28. Rall, J. A. *Mechanism of Muscular Contraction*. (Springer, New York, NY, 2014). doi:10.1007/978-1-4939-2007-5.

29. Fitts, R. H. The cross-bridge cycle and skeletal muscle fatigue. *J. Appl. Physiol.* 104, 551–558 (2007).

30. Gordon, A. M. *et al*. The variation in isometric tension with sarcomere length in vertebrate muscle fibres. *J. Physiol.* 184, 170–192 (1966).

31. Edman, K. A. *et al*. Residual force enhancement after stretch of contracting frog single muscle fibers. *J. Gen. Physiol.* 80, 769–784 (1982).

32. Shintani, S. A. *et al.* Sarcomere length nanometry in rat neonatal cardiomyocytes expressed with α-actinin–AcGFP in Z discs. *J. Gen. Physiol.* 143, 513–524 (2014).

33. Takekura, H. *et al*. Sequential docking, molecular differentiation, and positioning of T-Tubule/SR junctions in developing mouse skeletal muscle. *Dev. Biol.* 239, 204–214 (2001).

34. Hollingworth, S. & Baylor, S. M. Comparison of myoplasmic calcium movements during excitation–contraction coupling in frog twitch and mouse fast-twitch muscle fibers. *J. Gen. Physiol.* 141, 567–583 (2013).

35. Bartels, E. M. *et al*. The time course of the latency relaxation as a function of the sarcomere length in frog and mammalian muscle. *Acta Physiol. Scand.* 106, 129–137 (1979).

36. Dowling, J. J. *et al*. Triadopathies: An Emerging Class of Skeletal Muscle Diseases. *Neurotherapeutics* 11, 773–785 (2014).

37. Jungbluth, H. & Gautel, M. Pathogenic Mechanisms in Centronuclear Myopathies. *Front. Aging Neurosci.* 6, 339 (2014).

38. Dowling, J. J. *et al*. Molecular and cellular basis of genetically inherited skeletal muscle disorders. *Nat. Rev. Mol. Cell Biol.* 22, 713–732 (2021).

39. Hnia, K. *et al.* Myotubularin controls desmin intermediate filament architecture and mitochondrial dynamics in human and mouse skeletal muscle. *J. Clin. Invest.* 121, 70–85 (2011).

40. Durieux, A.-C. *et al.* A centronuclear myopathy-dynamin 2 mutation impairs skeletal muscle structure and function in mice. *Hum. Mol. Genet.* 19, 4820–4836 (2010).

41. Li, Q. *et al.* Dynamin-2 reduction rescues the skeletal myopathy of a SPEG-deficient mouse model. https://insight.jci.org/articles/view/157336/figure/2 (2022) doi:10.1172/jci.insight.157336.

42. Böhm, J. *et al.* Case report of intrafamilial variability in autosomal recessive centronuclear myopathy associated to a novel BIN1 stop mutation. *Orphanet J. Rare Dis.* 5, 35 (2010).

43. Razzaq, A. *et al.* Amphiphysin is necessary for organization of the excitation–contraction coupling machinery of muscles, but not for synaptic vesicle endocytosis in Drosophila. *Genes Dev.* 15, 2967–2979 (2001).

44. Nicot, A.-S. *et al.* Mutations in amphiphysin 2 (BIN1) disrupt interaction with dynamin 2 and cause autosomal recessive centronuclear myopathy. *Nat. Genet.* 39, 1134–1139 (2007).

45. Falcone, S. *et al.* N-WASP is required for Amphiphysin-2/BIN1-dependent nuclear positioning and triad organization in skeletal muscle and is involved in the pathophysiology of centronuclear myopathy. *EMBO Mol. Med.* 6, 1455–1475 (2014).

46. Pimentel, M. R. *et al*. In Vitro Differentiation of Mature Myofibers for Live Imaging. *J. Vis. Exp. JoVE* 55141 (2017) doi:10.3791/55141.

47. Schiaffino, S. & Margreth, A. COORDINATED DEVELOPMENT OF THE SARCOPLASMIC RETICULUM AND T SYSTEM DURING POSTNATAL DIFFERENTIATION OF RAT SKELETAL MUSCLE. *J. Cell Biol.* 41, 855–875 (1969).

48. Roman, W. & Gomes, E. R. Nuclear positioning in skeletal muscle. *Semin. Cell Dev. Biol.* 82, 51–56 (2018).

49. Grefte, S. *et al*. Matrigel, but not collagen I, maintains the differentiation capacity of muscle derived cells in vitro. *Biomed. Mater.* 7, 055004 (2012).

50. Slater, K. *et al*. Tuning the Elastic Moduli of Corning® Matrigel® and Collagen I 3D Matrices by Varying the Protein Concentration.

51. Hinds, S. *et al*. The role of extracellular matrix composition in structure and function of bioengineered skeletal muscle. *Biomaterials* 32, 3575–3583 (2011).

52. Engler, A. J. *et al.* Myotubes differentiate optimally on substrates with tissue-like stiffness: pathological implications for soft or stiff microenvironments. *J. Cell Biol.* 166, 877–887 (2004).

53. Jiwlawat, N. *et al.* Micropatterned substrates with physiological stiffness promote cell maturation and Pompe disease phenotype in human induced pluripotent stem cell-derived skeletal myocytes. *Biotechnol. Bioeng.* 116, 2377–2392 (2019).

54. Takahashi, H. *et al*. Engineered Human Contractile Myofiber Sheets as a Platform for Studies of Skeletal Muscle Physiology. *Sci. Rep.* 8, 13932 (2018).

55. Zhao, Y. *et al*. Fabrication of Skeletal Muscle Constructs by Topographic Activation of Cell Alignment. *Biotechnol. Bioeng.* 102, 10.1002/bit.22080 (2009).

56. Khademhosseini, A. *et al*. Microscale technologies for tissue engineering and biology. *Proc. Natl. Acad. Sci. U. S. A.* 103, 2480–2487 (2006).

57. Azioune, A. *et al*. Simple and rapid process for single cell micro-patterning. *Lab. Chip* 9, 1640 (2009).

58. Azioune, A. *et al*. Protein micropatterns: A direct printing protocol using deep UVs. *Methods Cell Biol.* 97, 133–146 (2010).

59. Vesga-Castro, C. *et al*. Contractile force assessment methods for in vitro skeletal muscle tissues. *eLife* 11, e77204 (2022).

60. Fambrough, D. M. Control of acetylcholine receptors in skeletal muscle. *Physiol. Rev.* 59, 165–227 (1979).

61. Herrmann-Frank, A. *et al*. Caffeine and excitation-contraction coupling in skeletal muscle: a stimulating story. *J. Muscle Res. Cell Motil.* 20, 223–237 (1999).

62. Dulhunty, A. F. Potassium contractures and mechanical activation in mammalian skeletal muscles. *J. Membr. Biol.* 57, 223–233 (1980).

63. Banan Sadeghian, R. *et al*. Electrical stimulation of microengineered skeletal muscle tissue: Effect of stimulus parameters on myotube contractility and maturation. *J. Tissue Eng. Regen. Med.* 12, 912–922 (2018).

64. Venturino, I. *et al.* Skeletal muscle cells opto-stimulation by intramembrane molecular transducers. *Commun. Biol.* 6, 1–11 (2023).

65. Sakar, M. S. *et al*. Formation and optogenetic control of engineered 3D skeletal muscle bioactuators. Lab Chip. 12, 4976-85 (2012).

66. Marcucci, L. Muscle Mechanics and Thick Filament Activation: An Emerging Two-Way Interaction for the Vertebrate Striated Muscle Fine Regulation. *Int. J. Mol. Sci.* 24, 6265 (2023).

67. Irving, M. Regulation of Contraction by the Thick Filaments in Skeletal Muscle. *Biophys. J.* 113, 2579–2594 (2017).

68. Xu, J. *et al.* In situ structural insights into the excitation contraction coupling mechanism of skeletal muscle. Preprint at https://doi.org/10.1101/2023.08.26.554922 (2023).

69. Stehbens, S. *et al*. Imaging intracellular protein dynamics by spinning disk confocal microscopy. *Methods Enzymol.* 504, 293–313 (2012).

70. York, A. G. *et al.* Instant super-resolution imaging in live cells and embryos via analog image processing. *Nat. Methods* 10, 1122–1126 (2013).

71. Hirano, M. *et al*. A highly photostable and bright green fluorescent protein. Nat Biotechnol. 40, 1412 (2022)

72. Zhovmer, A. & Combs, C. A. A Step-by-Step Guide to Instant Structured Illumination Microscopy (iSIM). in *Confocal Microscopy* (eds. Brzostowski, J. & Sohn, H.) vol. 2304 347–359 (2021).

73. Prakash, K. *et al*. Super-resolution microscopy: a brief history and new avenues. *Philos. Trans. R. Soc. Math. Phys. Eng. Sci.* 380, 20210110 (2022).

74. Brameshuber, M. *et al*. Understanding immune signaling using advanced imaging techniques. *Biochem. Soc. Trans.* 50, 853–866 (2022).

75. Petreanu, L. *et al*. The subcellular organization of neocortical excitatory connections. *Nature* 457, 1142–1145 (2009).

76. Chertkova, A. O. *et al.* Robust and Bright Genetically Encoded Fluorescent Markers for Highlighting Structures and Compartments in Mammalian Cells. Preprint at https://doi.org/10.1101/160374 (2017).

77. Shcherbakova, D. M. *et al.* Bright monomeric near-infrared fluorescent proteins as tags and biosensors for multiscale imaging. *Nat. Commun.* 7, 12405 (2016).

78. Fiji: an open-source platform for biological-image analysis | Nature Methods. https://www.nature.com/articles/nmeth.2019.

79. Roman, W. *et al.* Myofibril contraction and cross-linking drive nuclear movement to the periphery of skeletal muscle. *Nat. Cell Biol.* 19, 1189–1201 (2017).

80. Chen, Y. *et al.* Comparative assessment of the stability of nonfouling poly(2-methyl-2-oxazoline) and poly(ethylene glycol) surface films: an in vitro cell culture study. *Biointerphases* 9, 031003 (2014).

81. Riuzzi, F. *et al*. S100B Engages RAGE or bFGF/FGFR1 in Myoblasts Depending on Its Own Concentration and Myoblast Density. Implications for Muscle Regeneration. *PLOS ONE* 7, e28700 (2012).

82. Morin, A. *et al.* Dystrophin myonuclear domain restoration governs treatment efficacy in dystrophic muscle. *Proc. Natl. Acad. Sci. U. S. A.* 120, e2206324120 (2023).

83. Katti, P. *et al.* Mitochondrial network configuration influences sarcomere and myosin filament structure in striated muscles. *Nat. Commun.* 13, 6058 (2022).

84. DiFranco, M. *et al*. Optical Imaging and Functional Characterization of the Transverse Tubular System of Mammalian Muscle Fibers using the Potentiometric Indicator di-8-ANEPPS. *J. Membr. Biol.* 208, 141–153 (2005).

85. Uchida, K. & Lopatin, A. N. Diffusional and Electrical Properties of T-Tubules Are Governed by Their Constrictions and Dilations. *Biophys. J.* 114, 437–449 (2018).

86. Takekura, H. *et al.* Influences of sarcomere length and selective elimination of myosin filaments on the localization and orientation of triads in rat muscle fibres. *J. Muscle Res. Cell Motil.* 17, 235–242 (1996).

87. Moo, E. K. & Herzog, W. Single sarcomere contraction dynamics in a whole muscle. *Sci. Rep.* 8, 15235 (2018).

88. Tijs, C. *et al*. Effects of epimuscular myofascial force transmission on sarcomere length of passive muscles in the rat hindlimb. *Physiol. Rep.* 3, e12608 (2015).

89. Brown, I. E. *et al*. The effect of sarcomere length on triad location in intact feline caudofeomoralis muscle fibres. *J. Muscle Res. Cell Motil.* 19, 473–477 (1998).

90. Bagni, M. A. *et al*. Plateau and descending limb of the sarcomere length-tension relation in short length-clamped segments of frog muscle fibres. *J. Physiol.* 401, 581–595 (1988).

91. Kobirumaki-Shimozawa, F. *et al.* Synchrony of sarcomeric movement regulates left ventricular pump function in the in vivo beating mouse heart. *J. Gen. Physiol.* 153, e202012860 (2021).

92. Telley, I. A. *et al*. Half-Sarcomere Dynamics in Myofibrils during Activation and Relaxation Studied by Tracking Fluorescent Markers. *Biophys. J.* 90, 514–530 (2006).

93. Rausch, M. *et al.* Measurement of Skeletal Muscle Fiber Contractility with High-Speed Traction Microscopy. *Biophys. J.* 118, 657–666 (2020).

94. Hill, C. *et al*. Myosin-based regulation of twitch and tetanic contractions in mammalian skeletal muscle. *eLife* 10, e68211 (2021).

95. Bagnato, P. *et al*. Binding of an ankyrin-1 isoform to obscurin suggests a molecular link between the sarcoplasmic reticulum and myofibrils in striated muscles. *J. Cell Biol.* 160, 245–253 (2003).

96. Giacomello, E. *et al.* Deletion of small ankyrin 1 (sAnk1) isoforms results in structural and functional alterations in aging skeletal muscle fibers. *Am. J. Physiol.-Cell Physiol.* 308, C123–C138 (2015).

97. Trombitás, K. *et al.* Titin Extensibility In Situ: Entropic Elasticity of Permanently Folded and Permanently Unfolded Molecular Segments. *J. Cell Biol.* 140, 853–859 (1998).

98. Linke, W. A. *et al.* Towards a Molecular Understanding of the Elasticity of Titin. *J. Mol. Biol.* 261, 62–71 (1996).

99. Linke, W. A. *et al*. Nature of PEVK-titin elasticity in skeletal muscle. *Proc. Natl. Acad. Sci.* 95, 8052–8057 (1998).

100. Lu, F. *et al.* CMYA5 establishes cardiac dyad architecture and positioning. *Nat. Commun.* 13, 2185 (2022).

101. Kouloumenta, A. *et al*. Proper Perinuclear Localization of the TRIM-like Protein Myospryn Requires Its Binding Partner Desmin. *J. Biol. Chem.* 282, 35211–35221 (2007).

102. Sarparanta, J. *et al.* Interactions with M-band Titin and Calpain 3 Link Myospryn (CMYA5) to Tibial and Limb-girdle Muscular Dystrophies *. *J. Biol. Chem.* 285, 30304–30315 (2010).

103. Reynolds, J. G. *et al*. Deregulated Protein Kinase A Signaling and Myospryn Expression in Muscular Dystrophy*. *J. Biol. Chem.* 283, 8070–8074 (2008).

104. Tkatchenko, A. V. *et al.* Identification of altered gene expression in skeletal muscles from Duchenne muscular dystrophy patients. *Neuromuscul. Disord. NMD* 11, 269–277 (2001).

105. Kramerova, I. *et al.* Novel role of calpain-3 in the triad-associated protein complex regulating calcium release in skeletal muscle. *Hum. Mol. Genet.* 17, 3271–3280 (2008).

106. Gallardo, E. *et al*. Limb-girdle muscular dystrophy 2A. in *Handbook of Clinical Neurology* vol. 101 97–110 (Elsevier, 2011).

107. Ojima, K. *et al.* Non-proteolytic functions of calpain-3 in sarcoplasmic reticulum in skeletal muscles. *J. Mol. Biol.* 407, 439–449 (2011).

108. Fougerousse, F. *et al.* Expression of Genes (CAPN3, SGCA, SGCB, and TTN) Involved in Progressive Muscular Dystrophies during Early Human Development. *Genomics* 48, 145–156 (1998).

109. Hayashi, C. *et al.* Multiple Molecular Interactions Implicate the Connectin/Titin N2A Region as a Modulating Scaffold for p94/Calpain 3 Activity in Skeletal Muscle. *J. Biol. Chem.* 283, 14801–14814 (2008).

110. Huntoon, V. *et al.* SPEG-deficient skeletal muscles exhibit abnormal triad and defective calcium handling. *Hum. Mol. Genet.* 27, 1608–1617 (2018).

111. Lee, C. S. *et al.* Speg interactions that regulate the stability of excitation-contraction coupling protein complexes in triads and dyads. *Commun. Biol.* 6, 942 (2023).

112. Luo, S. *et al.* SPEG binds with desmin and its deficiency causes defects in triad and focal adhesion proteins. *Hum. Mol. Genet.* 29, 3882–3891 (2020).

113. Manring, H. R. *et al*. Obscure functions: the location–function relationship of obscurins. *Biophys. Rev.* 9, 245–258 (2017).

114. Sutter, S. B. *et al*. Orthologous relationship of obscurin and Unc-89: phylogeny of a novel family of tandem myosin light chain kinases. *Dev. Genes Evol.* 214, 352–359 (2004).

115. Qadota, H. *et al.* A Region of UNC-89 (Obscurin) Lying between Two Protein Kinase Domains Is a Highly Elastic Spring Required for Proper Sarcomere Organization. *J. Mol. Biol.* 432, 4799–4814 (2020).

116. Agrawal, P. B. *et al.* SPEG Interacts with Myotubularin, and Its Deficiency Causes Centronuclear Myopathy with Dilated Cardiomyopathy. *Am. J. Hum. Genet.* 95, 218–226 (2014).

117. Bang, M.-L. *et al.* Nebulin-deficient mice exhibit shorter thin filament lengths and reduced contractile function in skeletal muscle. *J. Cell Biol.* 173, 905–916 (2006).

118. Wang, *et al.* Identification of an N2 line protein of striated muscle. *Proc. Natl. Acad. Sci. U S A.* 77, 3254-8 (1980).